

This is an Open Access document downloaded from ORCA, Cardiff University's institutional repository: <https://orca.cardiff.ac.uk/id/eprint/167032/>

This is the author's version of a work that was submitted to / accepted for publication.

Citation for final published version:

Goold, Kameron, Seth, Anil, Molina, Mallory, Ohlson, David, Runnoe, Jessie C., Boker, Torsten, Davis, Timothy A., Dumont, Antoine, Eracleous, Michael, Fernandez-Ontiveros, Juan Antonio, Gallo, Elena, Goulding, Andy D., Greene, Jenny E., Ho, Luis C., Markoff, Sera B., Neumayer, Nadine, Plotkin, Richard M., Prieto, Almudena, Satyapal, Shobita, van de Ven, Glenn, Walsh, Jonelle L., Yuan, Feng, Feldmeier-Krause, Anja, Gultekin, Kayhan, Honig, Sebastian, Kirkpatrick, Allison, Lutzgendorf, Nora, Reines, Amy E., Strader, Jay, Trump, Jonathan R. and Voggel, Karina T. 2024. ReveaLLAGN 0: First look at JWST MIRI data of Sombrero and NGC 1052. *Astrophysical Journal*

Publishers page:








Please note:

Changes made as a result of publishing processes such as copy-editing, formatting and page numbers may not be reflected in this version. For the definitive version of this publication, please refer to the published source. You are advised to consult the publisher's version if you wish to cite this paper.

This version is being made available in accordance with publisher policies. See <http://orca.cf.ac.uk/policies.html> for usage policies. Copyright and moral rights for publications made available in ORCA are retained by the copyright holders.



ReveaLLAGN 0: First Look at JWST MIRI data of Sombrero and NGC 1052

1 KAMERON GOOLD ¹ ANIL SETH ¹ MALLORY MOLINA ^{1,2} DAVID OHLSON ¹ JESSIE C. RUNNOE ²
2 TORSTEN BÖKER ³ TIMOTHY A. DAVIS ⁴ ANTOINE DUMONT ⁵ MICHAEL ERACLEOUS ⁶
3 JUAN ANTONIO FERNÁNDEZ-ONTIVEROS ^{7,8} ELENA GALLO ⁹ ANDY D. GOULDING ¹⁰ JENNY E. GREENE ¹⁰
4 LUIS C. HO ^{11,12} SERA B. MARKOFF ¹³ NADINE NEUMAYER ⁵ RICHARD M. PLOTKIN ^{14,15}
5 ALMUDENA PRIETO ^{16,17,18} SHOBITA SATYAPAL ¹⁹ GLENN VAN DE VEN ²⁰ JONELLE L. WALSH ²¹ FENG YUAN ²²
6 ANJA FELDMEIHER-KRAUSE ⁵ KAYHAN GÜLTEKIN ⁹ SEBASTIAN HÖNIG ²³ ALLISON KIRKPATRICK ²⁴
7 NORA LÜTZGENDORF ³ AMY E. REINES ²⁵ JAY STRADER ²⁶ JONATHAN R. TRUMP ²⁷ AND
8 KARINA T. VOGGEL ²⁸

9 ¹*Department of Physics & Astronomy, University of Utah, James Fletcher Building, 115 1400 E, Salt Lake City, UT 84112, USA*

10 ²*Department of Physics & Astronomy, Vanderbilt University, Nashville, TN 37235, USA*

11 ³*European Space Agency, c/o STScI, 3700 San Martin Drive, Baltimore, MD 21218, USA*

12 ⁴*Cardiff Hub for Astrophysics Research & Technology, School of Physics & Astronomy, Cardiff University, Queens Buildings, Cardiff,*
13 *CF24 3AA, UK*

14 ⁵*Max-Planck-Institut für Astronomie, Königstuhl 17, D-69117, Heidelberg, Germany*

15 ⁶*Department of Astronomy & Astrophysics and Institute for Gravitation and the Cosmos, The Pennsylvania State University, 525 Davey*
16 *Lab, University Park, PA 16802, USA*

17 ⁷*Istituto di Astrofisica e Planetologia Spaziali (INAF-IAPS), Via Fosso del Cavaliere 100, I-00133 Roma, Italy*

18 ⁸*Centro de Estudios de Física del Cosmos de Aragón (CEFCA), Plaza San Juan 1, E-44001, Teruel, Spain*

19 ⁹*Department of Astronomy, University of Michigan, 1085 S. University Ave., Ann Arbor, MI 48109, USA*

20 ¹⁰*Department of Astrophysical Sciences, Princeton University, Princeton, NJ 08544, USA*

21 ¹¹*Kavil Institute for Astronomy and Astrophysics, Peking University, Beijing 100871, China*

22 ¹²*Department of Astronomy, School of Physics, Peking University, Beijing 100871, China*

23 ¹³*Anton Pannekoek Institute for Astronomy, University of Amsterdam, Science Park 904, 1098 XH Amsterdam, The Netherlands*

24 ¹⁴*Department of Physics, University of Nevada, Reno, NV 89557, USA*

25 ¹⁵*Nevada Center for Astrophysics, University of Nevada, Las Vegas, NV 89154, USA*

26 ¹⁶*Universidad de La Laguna (ULL), Dpto. Astrofísica, Avd. Astrofísico Fco. Sánchez s/n, 38206 La Laguna, Tenerife, Spain*

27 ¹⁷*Instituto de Astrofísica de Canarias (IAC), C/Vía Láctea s/n, 38205 La Laguna, Tenerife, Spain*

28 ¹⁸*Universitäts-Sternwarte, Fakultät für Physik, Ludwig-Maximilians-Universität München, 81679 München, Germany*

29 ¹⁹*George Mason University, Department of Physics and Astronomy, MS3F3, 4400 University Drive, Fairfax, VA 22030, USA*

30 ²⁰*Department of Astrophysics, University of Vienna, Türkenschanzstraße 17, 1180 Vienna, Austria*

31 ²¹*George P. and Cynthia W. Mitchell Institute for Fundamental Physics and Astronomy, Department of Physics & Astronomy, Texas*
32 *A&M University, 4242 TAMU, College Station, TX 77843, USA*

33 ²²*Shanghai Astronomical Observatory, Chinese Academy of Sciences, Shanghai 200030, People's Republic of China*

34 ²³*Department of Physics & Astronomy, University of Southampton, Hampshire SO17 1BJ Southampton, UK*

35 ²⁴*Department of Physics and Astronomy, University of Kansas, Lawrence, KS 66045, USA*

36 ²⁵*eXtreme Gravity Institute, Department of Physics, Montana State University, Bozeman, MT 59717, USA*

37 ²⁶*Department of Physics and Astronomy, Michigan State University, East Lansing, MI 48824, USA*

38 ²⁷*Department of Physics, 196 Auditorium Road, Unit 3046, University of Connecticut, Storrs, CT 06269, USA*

39 ²⁸*Universite de Strasbourg, CNRS, Observatoire astronomique de Strasbourg, UMR 7550, 67000 Strasbourg, France*

ABSTRACT

41 We present the first results from the Revealing Low-Luminosity Active Galactic Nuclei (ReveaL-
42 LAGN) survey, a JWST survey of seven nearby LLAGN. We focus on two observations with the
43 Mid-Infrared Instrument's (MIRI) Medium Resolution Spectrograph (MRS) of the nuclei of NGC 1052
44 and Sombrero (NGC 4594 / M104). We also compare these data to public JWST data of a higher-
45 luminosity AGN, NGC 7319 and NGC 7469. JWST clearly separates the AGN spectrum from the
46 galaxy light even in Sombrero, the faintest target in our survey; the AGN components have very red
47 spectra. We find that the emission-line widths in both NGC 1052 and Sombrero increase with in-
48 creasing ionization potential, with FWHM > 1000 km s⁻¹ for lines with ionization potential $\gtrsim 50$ eV.
49 These lines are also significantly blue-shifted in both LLAGN. The high ionization potential lines in

NGC 7319 show neither broad widths or significant blue shifts. Many of the lower ionization potential emission lines in Sombrero show significant blue wings extending $>1000 \text{ km s}^{-1}$. These features and the emission-line maps in both galaxies are consistent with outflows along the jet direction. Sombrero has the lowest luminosity high-ionization potential lines ([Ne V] and [O IV]) ever measured in the mid-IR, but the relative strengths of these lines are consistent with higher luminosity AGN. On the other hand, the [Ne V] emission is much weaker relative to the [Ne III] and [Ne II] lines of higher-luminosity AGN. These initial results show the great promise that JWST holds for identifying and studying the physical nature of LLAGN.

1. INTRODUCTION

As material falls onto a black hole, that material heats up and emits light creating an active galaxy nucleus (AGN). While the most rapidly accreting objects are seen to the edges of our Universe as luminous quasars, the vast majority of central supermassive black holes in nearby galaxies are accreting at less than 1% of their Eddington Limit ($L_{\text{bol}}/L_{\text{Edd}} < 0.01$; see Ho 2009). These low-luminosity AGN (LLAGN) are theorized to have significantly different inner structures from the accretion disks found in more luminous AGN.

At these low accretion rates, the inner part of the optically thick accretion disk transitions to a hot, optically thin, radiatively inefficient accretion flow (RIAF; Narayan & Yi 1995; Yuan & Narayan 2014; Porth et al. 2019). This change in the central regions of LLAGN will result in a different ionizing spectrum with fewer far-ultraviolet photons.

Observationally, this is confirmed by the lack of the “big blue bump” in LLAGN spectral energy distributions (SEDs; Ho 1999). This change in ionizing flux is also expected to be reflected in the optical emission line strengths. Enhanced low ionization emission lines are a key characteristic of low ionization nuclear emission regions (LINERs) which were first identified by Heckman (1980) based solely on optical oxygen lines. LINERs are notably diverse, including sources both with and without clear evidence of an AGN. Multiple radio and X-ray surveys have consistently revealed that most LINERs are powered by LLAGNs (Nagar et al. 2002, 2005; Filho et al. 2006; Dudik et al. 2005; Flohic et al. 2006; González-Martín et al. 2006, 2009; Ho 2008; Hernández-García et al. 2013, 2014). However, LLAGNs are not coincident with LINERs exclusively, many weakly accreting Seyferts are also considered LLAGNs (Kewley et al. 2006; Ho 2009). Optical classification notwithstanding, LLAGNs share additional observational signatures. In particular, the dusty torus and broad line region components may disappear (e.g. Plotkin et al. 2012; Elitzur et al. 2014); and as the Eddington Ratio decreases, LLAGN tend to have stronger jet emission (Ho 2008) and become increasingly radio-loud (Ho 2002; Terashima & Wilson 2003; Greene et al. 2006; Panessa

et al. 2007; Sikora et al. 2007; Trump et al. 2011). The kinetic energy injected into LLAGN host galaxies by jets may play a significant role in keeping massive early-type galaxies quiescent (Croton et al. 2006; Weinberger et al. 2017). Despite these observational signatures the inner structure of LLAGNs are still not yet well understood and it becomes increasingly difficult to separate out the low luminosity nuclear emission of weakly accreting AGN from the surrounding light and obscuring dust of the host galaxy.

Infrared (IR) wavelengths are particularly valuable for studying AGN (Sajina et al. 2022), as the dust that hides many AGN at optical and UV wavelengths strongly emits in the IR. In fact, the energy output for many AGN is highest at X-ray and mid-IR wavelengths (Prieto et al. 2010). Furthermore, the emission from AGN at $12 \mu\text{m}$ has been found to be tightly correlated with the 2–10 keV X-ray emission, with similar luminosities in both bands (Asmus et al. 2015). In addition to the continuum emission from dust or jet emission (e.g. Prieto et al. 2016; Fernández-Ontiveros et al. 2023), strong emission lines are seen at infrared wavelengths, including high ionization potential (IP) “coronal” emission lines that track the ionizing spectrum of the AGN (e.g. Satyapal et al. 2008; Goulding & Alexander 2009).

JWST, operating primarily in the IR, is equipped with advanced instruments and brings new opportunities in the study of AGN. The brightness of AGN in the IR beyond 2 microns combined with JWST’s unprecedented sensitivity at these wavelengths makes it the most sensitive instrument ever for detecting AGN. For example, the depth reached in just 10 ks of Mid-Infrared Instrument (MIRI) imaging at 12 microns roughly matches that of 2 Ms from Chandra Deep Field North (Xue et al. 2016, assuming the Asmus et al. (2015) relation between the mid-IR and X-ray emission). The remarkable spatial resolution afforded by JWST’s 6.5-meter diameter mirror allows us to isolate the LLAGN emission from that of the host galaxy in nearby objects. Finally, JWST’s spectral resolution enables studies of line emission profiles that were not possible with previous missions.

The Revealing LLAGN (ReveaLLAGN) project, utilizing integral field spectroscopic (IFS) observations

144 from JWST, aims to achieve two primary goals. The
 145 first is to provide templates of LLAGN spectra, which
 146 can be used to identify the abundant faint AGN hidden
 147 in future JWST data of local and high-redshift galaxies.
 148 This includes environments where their presence is cur-
 149 rently uncertain, e.g. in dwarf galaxies. Second, through
 150 the analysis of the continuum and coronal-line emissions,
 151 the project aims to offer valuable constraints for under-
 152 standing the internal structure of LLAGN. The study
 153 focuses on seven nearby, well-known LLAGN covering
 154 a wide range of both black hole mass ($10^{5.5-9.8} M_{\odot}$)
 155 and Eddington ratio ($\log(L_{bol}/L_{edd})$ ranging from -6.2
 156 to -2.7).

157 In this paper, we report the first results from the
 158 ReveaLLAGN project based on the MIRI medium-
 159 resolution spectrometer (MRS) data from our first two
 160 targets, Sombrero (also known as M104 and NGC 4594)
 161 and NGC 1052. The overall properties of these galaxies
 162 are listed in Table 1. These two galaxies have the highest
 163 (NGC 1052) and lowest (Sombrero) $12 \mu\text{m}$ fluxes (Asmus
 164 et al. 2014) of all the galaxies in the full ReveaLLAGN
 165 sample (Seth et al., *in prep*), and thus represent the
 166 full range of signal-to-noise ratios (S/N) expected for
 167 the survey. NGC 1052 and Sombrero are classified as
 168 LINERs based on their optical emission lines (Heckman
 169 1980; Ho et al. 1997)¹ and exhibit extensive multiwave-
 170 length emission from their LLAGN. Hard X-ray observa-
 171 tions reveal point sources in the center of both galaxies
 172 (NGC1052: Guainazzi & Antonelli 1999; Kadler et al.
 173 2004b; Sombrero: Fabbiano & Juda 1997; Pellegrini
 174 et al. 2002, 2003), accompanied by UV variability (Maoz
 175 et al. 2005). In the radio domain, NGC 1052 hosts jets
 176 at parsec scales with a position angle of ~ 70 degrees
 177 (Claussen et al. 1998; Kadler et al. 2004b), while at kilo-
 178 parsec scales the PA of the radio jets are seen at ~ 100
 179 degrees Wrobel (1984); Kadler et al. (2004a). The Som-
 180 brero Galaxy also contains compact jets, observed at
 181 sub-parsec scales with a PA of -25 degrees (Hada et al.
 182 2013). Additionally, both AGNs’ SEDs show a lack of
 183 emission in the UV relative to higher luminosity AGN
 184 (Fernández-Ontiveros et al. 2023), consistent with other
 185 LLAGN (Ho 2008). We review previous observations of
 186 both galaxies’ AGN in more depth in Section 5.3.

187 We contrast these two LLAGN observations with pre-
 188 vious Spitzer data of higher luminosity AGN. We also
 189 include JWST MIRI/MRS observations of NGC 7319
 190 (part of the JWST Early Release Observations; Pontop-
 191 pidan et al. 2022) and NGC 7469 (Armus et al. 2023),

¹ We note that the line ratios of NGC 1052 depends on radius, and are Seyfert-like at smaller radii (Molina et al. 2018)

192 two Seyfert galaxies with higher luminosity and Edding-
 193 ton ratios than our targets. The 2-10 keV X-ray lumi-
 194 nosities of NGC 7319 and NGC 7469 are $10^{43.1} \text{ erg s}^{-1}$
 195 and $10^{43.2} \text{ erg s}^{-1}$ (Ricci et al. 2017). Their BH mass
 196 estimates are $10^{8.1} M_{\odot}$ and $10^7 M_{\odot}$ and their Eddington
 197 ratios are -1.67 / -0.72 (Koss et al. 2022). Both galax-
 198 ies are part of interacting systems and are at larger dis-
 199 tances (98.3 Mpc and 69.4 Mpc) than our ReveaLLAGN
 200 sample. Despite the increased distances, the higher lu-
 201 minosity results in a physically larger line-emitting re-
 202 gion dominated by AGN photoionization, which helps to
 203 mitigate the differences in physical length scales between
 204 them and our sample. The nuclear spectra of NGC 7319
 205 and NGC 7469 are AGN dominated and point-like at
 206 MIRI wavelengths, representing suitable examples of
 207 higher luminosity AGN with similar spectral resolution
 208 and wavelength coverage as our ReveaLLAGN targets.

209 In Section 2 we describe the data acquisition and re-
 210 duction processes. We present our spectral extraction
 211 process and emission-line measurements for both the nu-
 212 clear spectra and the emission-line maps in Section 3.
 213 We present our analysis of the data in Section 4, and
 214 discuss them in context of previous work in Section 5.
 215 We conclude in Section 6. We note that all JWST data
 216 is barycenter corrected, and thus velocities are given in
 217 the barycentric frame.

218 2. DATA REDUCTION AND METHODS

219 2.1. Targets and Data Acquisition

220 We use JWST MIRI/MRS (Wells et al. 2015) to col-
 221 lect IFS data for our ReveaLLAGN targets in the mid-
 222 IR (4.9–27.9 μm). The full mid-IR wavelength range
 223 for MIRI/MRS is covered by 4 different channels (ch1–
 224 4): ch1 (4.9–7.65 μm) and ch2 (7.51–11.71 μm) use the
 225 MIRIFU.SHORT Detector, while ch3 (11.55–17.98 μm)
 226 and ch4 (17.71–27.9 μm) use the MIRIFU.LONG Detec-
 227 tor. Each channel has an increasing field of view (FoV):
 228 ch1 ($3.2'' \times 3.7''$), ch2 ($4.0'' \times 4.8''$), ch3 ($5.2'' \times 6.2''$),
 229 and ch4 ($6.6'' \times 7.7''$), and pixel size: ch1 ($0''.196$), ch2
 230 ($0''.196$), ch3 ($0''.245$), ch4 ($0''.273$). All observations were
 231 taken using all three MIRI/MRS sub-channels.

232 We describe the observational details for our two Re-
 233 veaLLAGN targets; details on the NGC 7319 observa-
 234 tion are discussed in (Pereira-Santaella et al. 2022). Our
 235 Sombrero observations are centered at RA: 12:39:59.430
 236 DEC: -11:37:22.99; this is taken from Gaia EDR3 (Gaia
 237 Collaboration et al. 2021). Our NGC 1052 observations
 238 are centered at RA: 02:41:04.798, DEC: -08:15:20.75
 239 taken from very-long-baseline interferometry measure-
 240 ments of the AGN (Lambert & Gontier 2009).

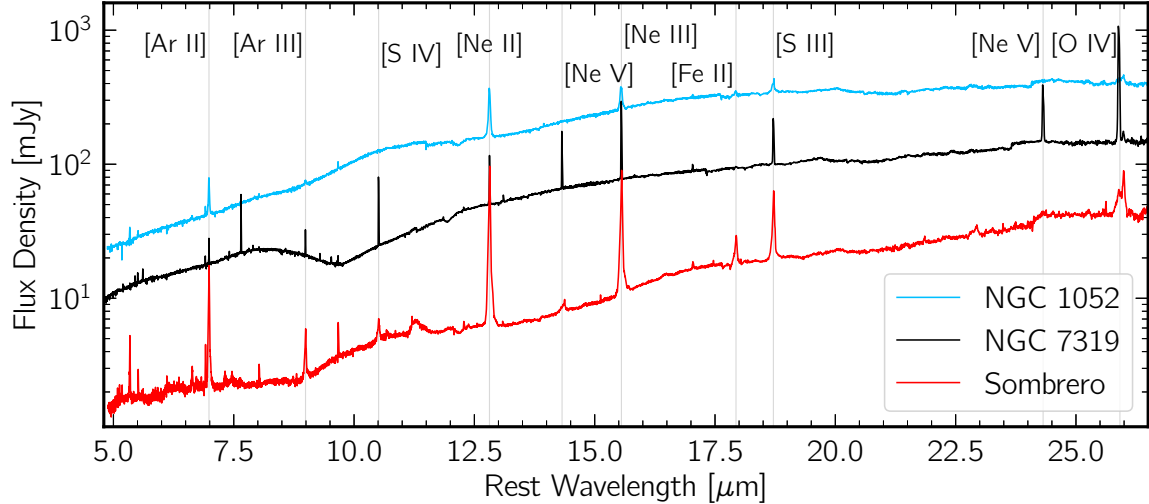


Figure 1. The first extracted nuclear spectra of ReveaLLAGN targets: Sombrero (red, bottom spectrum) and NGC 1052 (blue, top spectrum). NGC 7319 (black, middle spectrum) is a more distant and more luminous Seyfert 2 AGN and is included to compare our low-luminosity sample to another spectrum taken with JWST MIRI/MRS. Spectra are extracted from a ~ 1 FWHM radius aperture (see Section 3.1) and are aperture corrected using point source observations. A subset of strong emission lines are labeled. Also apparent in the spectra at ~ 10 microns are broad Silicate absorption features (in NGC 7319) and emission features (in Sombrero and NGC 1052), and faint polycyclic aromatic hydrocarbon (PAH) emission at $11.3 \mu\text{m}$ in Sombrero.

Table 1. Galaxy Properties

Galaxy Name	Distance Mpc	V_{sys} km s^{-1}	Galaxy Mass $\log(M_*/M_\odot)$	Morph.	AGN Type	BH Mass $\log(M_\bullet/M_\odot)$	AGN X-ray Lum. $\log(L_X/\text{erg s}^{-1})$	Eddington Ratio $\log(L_{bol}/L_{edd})$
NGC 1052	19.4 ± 0.2	1487.9 ± 5.1	10.71	E4	L1.9	8.82	41.46	-3.97
Sombrero/M104/NGC 4594 ¹	9.6 ± 0.3	1090.9 ± 5.1	11.18	Sa	L2	8.83	40.04	-5.66

References— Distances: NGC 1052 – Tonry et al. (2001), Sombrero – McQuinn et al. (2016). **Systemic Velocities** V_{sys} : are NASA Extragalactic database heliocentric velocities taken from Fouque et al. (1992) for NGC 1052 and de Vaucouleurs et al. (1991) for Sombrero. **Galaxy Mass:** NGC 1052 & Sombrero from S4G (Sheth et al. 2010; Eskew et al. 2012) with Sombrero corrected to the distance used here. **Morphological Type:** from de Vaucouleurs et al. (1991), **AGN Type:** NGC 1052 and Sombrero from Ho et al. (1997). **BH Mass:** NGC 1052 is based on velocity dispersion (Koss et al. 2022), Sombrero from Jardel et al. (2011). **AGN X-ray Luminosity:** 2-10 keV luminosities for NGC 1052 from Koss et al. (2022), Sombrero from Fernández-Ontiveros et al. (2023) using updated distance. **Eddington Ratio:** NGC 1052 and Sombrero from Fernández-Ontiveros et al. (2023) using listed distances and BH masses.

¹We adopt “Sombrero” for the galaxy’s name in this work.

241 Background exposures were taken using offset blank
242 fields selected based on WISE $12 \mu\text{m}$ imaging: for
243 Sombrero this field was at RA: 12:39:55.9810, DEC:
244 $-11:32:11.44$ and for NGC 1052 at RA: 02:41:5.1200,
245 DEC: $-08:12:37.70$.

246 Our MIRI/MRS measurements were taken using the
247 4-Point, Extended Source optimized ALL-channel dither
248 pattern using the inverted, or negative, dither orienta-
249 tion². This ensures improved sampling of the point

² <https://jwst-docs.stsci.edu/jwst-mid-infrared-instrument/miri-operations/miri-dithering/miri-mrs-dithering>

250 spread function (PSF) at all wavelengths and allows the
251 correction of hot detector pixels. The exposure time for
252 both Sombrero and NGC 1052 was 921.313 seconds split
253 over four dithers for each sub-channel setting. Back-
254 ground exposures used a single dither position with an
255 exposure length of 230.328 seconds for each sub-channel
256 setting. The Sombrero data were among the first sci-
257 ence data taken with JWST on July 4th, 2022, while
258 the NGC1052 data were taken on August 11th, 2022.

259 The JWST data presented in this paper were ob-
260 tained from the Mikulski Archive for Space Telescopes
261 (MAST) at the Space Telescope Science Institute. The

specific observations analyzed can be accessed via DOI:
10.17909/n1hq-4p52.

2.2. Data Reduction

We process the raw observations for Sombrero, NGC 1052, and NGC 7319 through version 1.8.2 of the JWST pipeline (Bushouse et al. 2022) using `jwtst_0989.pmap`, which is a versioned reference file that gives overall context for the pipeline. Calibration of our data is divided into three main stages of processing; the `Detector1`, `Spec2`, and `Spec3` pipelines.

The `Detector1` pipeline takes the raw counts from the detector, applies basic detector-level corrections to all exposures, and creates uncalibrated countrate images, or `lvl2a` data products³. The `Spec2` pipeline takes the `lvl2a` products and applies additional instrumental corrections and calibrations to produce a fully calibrated individual exposure, or `lvl2b` data products. For MIRI/MRS observations, this stage includes adding WCS information, flat field corrections, and stray light subtraction. We include an optional fringing removal⁴ step during this stage to address the significant fringes found in the MIRI/IFU data. The `Spec3` pipeline processes `lvl2b` spectroscopic observations into `lvl3` data by combining calibrated `lvl2b` data from associated dithered exposures into a 3-D spectral cube or 2-D extracted spectra. For MIRI/MRS data the master background subtraction and outlier detection occurs in this stage as well. We choose a final product of 4 data cubes, one for each channel⁵. The wavelength solution, FLT-4, associated with our pipeline version has a 1σ wavelength calibration error of 10–30 km s⁻¹ (Argyriou et al. 2023) through the MRS wavelength range.

3. SPECTRAL EXTRACTION AND METHODS

3.1. Nuclear Spectra Extraction

Nuclear spectra were extracted using the `photutils` python package’s aperture photometry code. At each wavelength, we used a photometric aperture centroided on the median flux image of each channel. The width of this aperture depended on wavelength to account for the changing PSF, with an angular radius of $1.22\lambda/(6.5 \text{ meters})$ – roughly 1 spatial FWHM ($\text{FWHM}_{\text{Rayleigh}}$); this aperture radius ranges from 0’19 at 5 μm to 0’97 at 25 μm . The radius of this aperture on the short wavelength 0’19 corresponds to 8.8, 17.9, and 92 pc in Sombrero, NGC 1052, and NGC 7319 respectively. Back-

³ See [calwebb_detector1 documentation](#) for more information.

⁴ See [calwebb_spec2 documentation](#) for more information

⁵ See [calwebb_spec3 documentation](#) for more information.

ground subtraction was done using an annulus with radii between 2 and $2.5\times$ this value.

We created a wavelength-dependent aperture correction based on the MIRI data cube of 10 Lac (obtained from Argyriou, I., *private communication*). This aperture correction (total/aperture flux) was derived using the same aperture and background annulus as for our galaxy nuclei, with the total flux obtained by integrating the flux of the full data cube. Due to residual sky background issues, we took the median flux of pixels with a radius greater than $6\times\text{FWHM}_{\text{Rayleigh}}$ as a background subtraction in each spaxel before calculating the total flux of the data cube at each wavelength. To create a smooth relation, we smoothed the derived aperture correction at each wavelength with a moving median. We compared this smoothed aperture correction to several other point source observations (HD192163 and HD76534) as well as NGC 1052, which is nearly point like at longer wavelengths and found generally good agreement (to within $\sim 10\%$) in the aperture corrections between sources for channels 1-3, with much poorer agreement and due to noisier measurements in channel 4. The aperture correction declines from values of ~ 2.1 at 5 μm to values similar to the `WebbPSF` prediction (1.4). We therefore fit a 5th order polynomial to our smoothed correction in channels 1-3, and set the `ch4` correction to a constant 1.4 value. This aperture correction has been applied throughout this paper.

3.2. Measuring Emission Features

3.2.1. Multi-Gaussian Fitting of the Nuclear Spectrum

Our nuclear spectra are very high S/N with clear evidence of many emission lines. These lines often show complex profiles – to extract both flux and velocity information from these lines, we perform multi-Gaussian fits. We first define continuum and fitting windows for each line based on visual inspection – our default fitting window is based on a velocity width of 5000 km s⁻¹. We fit a linear function to the continuum on either side of the emission feature and subtract the result from the data. Next, we utilize the python package `lmfit` to fit both a single Gaussian and multi-Gaussian model to the continuum-subtracted emission line. We allow the multi-Gaussian model to consist of up to five components, where each Gaussian component is constrained by the width of the wavelength dependent MIRI instrument LSF and the results of the initial single-Gaussian fits. We select the model with the lowest Bayesian inference criteria (BIC) as the best-fit model. An example fit to [Fe II] $\lambda 5.34 \mu\text{m}$ is shown in the left panel of Figure 2. We do not ascribe any physical interpretation to the individual Gaussian components, instead, we use them to

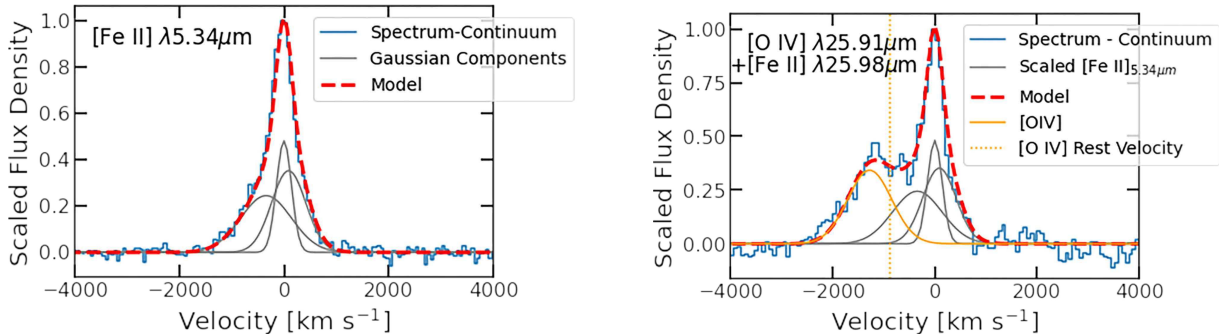


Figure 2. Two examples from Sombrero of the multi-Gaussian models used to characterize emission lines in our sample. *Left* – The [Fe II] $\lambda 5.34 \mu\text{m}$ emission-line fit with a three-component Gaussian model. The gray lines represent individual Gaussian components, while the red dashed line is the sum of those three components. This is the typical method used for characterizing emission features in our data. *Right* – One of the two coronal lines requiring deblending; here we show the [O IV] $\lambda 25.91 \mu\text{m}$ line, which is blended with [Fe II] $\lambda 25.98 \mu\text{m}$; a scaled version of the [Fe II] $\lambda 5.34 \mu\text{m}$ line is fit along with a single Gaussian for the [O IV] line. All components are plotted relative to the velocity of [Fe II] $\lambda 25.98 \mu\text{m}$. Markings are as in the left panel, with [O IV] and its expected rest velocity shown in orange.

358 accurately describe the emission-line profile from which
 359 we measure the flux, peak velocity, and $\text{FWHM}_{\text{model}}$.
 360 The $\text{FWHM}_{\text{line}}$ of each emission-line is corrected for the
 361 width of the MIRI/MRS line spread function (LSF) at
 362 the corresponding wavelength, given by

$$363 \quad \text{FWHM}_{\text{line}} = \sqrt{\text{FWHM}_{\text{model}}^2 - \text{FWHM}_{\text{LSF}}^2} \quad (1)$$

364 We use the MIRI MRS LSF width given by Argyriou
 365 et al. (2023): $\text{FWHM}_{\text{LSF}} = c/R$, where c is the speed of
 366 light, and $R = 4603 - 128\lambda$.

367 Errors on derived quantities are determined from
 368 a Monte Carlo (MC) simulation with Gaussian noise
 369 added to each pixel based on the standard deviation of
 370 the pixels in the continuum windows. The median stan-
 371 dard deviation in the continuum pixels is $\sim 4\times$ the for-
 372 mal flux errors provided by the pipeline. Emission-line
 373 detections are determined if the integrated flux of the
 374 best single-Gaussian emission-line model is above a 5σ
 375 threshold. 5σ upper limits are provided for lines without
 376 clear detections. We adopt a lower limit on errors for any
 377 wavelength dependent measurement equal to the wave-
 378 length calibration error of 30 km s^{-1} provided in 2.2.
 379 The derived line properties and their associated errors
 380 are given in Table 2.

381 Two key lines of interest for tracing AGN activity are
 382 the high-IP lines (IP > 50 eV) [Ne V] $\lambda 14.32 \mu\text{m}$ and
 383 [O IV] $\lambda 25.91 \mu\text{m}$. However in both our ReveLLAGN
 384 targets, these lines are each blended with a neighbor-
 385 ing low-IP line (IP < 20). Specifically, [Ne V] $\lambda 14.32 \mu\text{m}$ is
 386 blended with the [Cl II] $\lambda 14.36 \mu\text{m}$ emission line, while
 387 [O IV] $\lambda 25.91 \mu\text{m}$ is blended with the [Fe II] $\lambda 25.98 \mu\text{m}$
 388 emission line. We deblend the features using a con-
 389 strained multi-Gaussian model; the low-IP component
 390 is fixed to be a scaled version of the [Fe II] $\lambda 5.34 \mu\text{m}$ line

391 (Figure 2), an isolated low-IP line with high signal-to-
 392 noise. We then allow `lmfit` to fit the [Ne V] $\lambda 14.32 \mu\text{m}$
 393 and [O IV] $\lambda 25.91 \mu\text{m}$ emission with a single Gaus-
 394 sian component. To capture the full uncertainty of
 395 this measurement we fit the [Fe II] $\lambda 5.34 \mu\text{m}$ in each
 396 iteration of the MC process before constraining the
 397 [Ne V] $\lambda 14.32 \mu\text{m}$ and [O IV] $\lambda 25.91 \mu\text{m}$ models.

3.2.2. Constructing Emission Line Maps

398
 399 Outside the nucleus, many lines have low signal-to-
 400 noise ratios, making the multi-Gaussian method we use
 401 for the nuclear spectrum less robust. We therefore sim-
 402 plify the Gaussian fitting process used for the nuclear
 403 spectra described above by limiting the Gaussian model
 404 to a single Gaussian component. The emission-line flux
 405 is calculated by measuring the area under the best-fit
 406 Gaussian model, while velocity is determined by calcu-
 407 lating the displacement between the centroid of the best-
 408 fit Gaussian model and the rest wavelength of the emis-
 409 sion line. For the blended high-IP features (e.g. Fig. 2,
 410 right), we attempted to deblend them pixel-by-pixel us-
 411 ing two-Gaussian fits, but found no significant detection
 412 of the [Ne V] $\lambda 14.32 \mu\text{m}$ and [O IV] $\lambda 25.91 \mu\text{m}$ emission
 413 beyond the central few spaxels due to a combination of
 414 low S/N and perhaps the nuclear concentration of these
 415 lines. We calculate errors on the flux and velocity using
 416 a Monte Carlo simulation as above, and use a 5σ de-
 417 tection threshold, below which we find our Gaussian fits
 418 don’t characterize the data well. We discuss the result-
 419 ing line maps in the Section 4.2.1.

420 To investigate the ionizing mechanisms of our emission
 421 lines, we quantify the spatial extent of the emission re-
 422 gion in our line maps by measuring the spatial FWHM
 423 ($\text{FWHM}_{\text{spat}}$) of prominent emission lines. We do this
 424 by creating a contour at 50% of the peak flux and cal-

425 culate $2\times$ the median radius from the peak flux to the
 426 contour line. We correct the measured $\text{FWHM}_{\text{spat}}$ for
 427 the MIRI/MRS PSF, which varies by a factor of five
 428 over the MIRI wavelength range. Using the FWHM of
 429 the MIRI/MRS PSF (FWHM_{MRS}) taken from [Argyriou](#)
 430 [et al. \(2023\)](#) we get:

$$431 \quad \text{FWHM}_{\text{spat,corr}} = \sqrt{\text{FWHM}_{\text{spat}}^2 - \text{FWHM}_{\text{MRS}}^2} \quad (2)$$

432 The results for this measurement are listed in Table 3
 433 and presented in Section 4.2.2, with discussion in 5.2.

434 4. RESULTS

435 4.1. Nuclear Region Emission Line Analysis

436 4.1.1. Variations with Ionization Potential

437 In Figure 3 we show the nuclear emission-line prop-
 438 erties in our two ReveLLAGN targets, as well as
 439 NGC 7319, ordered by their IP to search for system-
 440 atic trends. The top panel shows the line luminosity
 441 and we find the most luminous detected lines in Som-
 442 brero and NGC 1052 are [Ne II] $\lambda 12.81 \mu\text{m}$ followed by
 443 [Ne III] $\lambda 15.56 \mu\text{m}$ which have IPs of 21.56 and 40.96 eV
 444 respectively, while in NGC 7319 the [O IV] $\lambda 25.91 \mu\text{m}$
 445 line (IP=54.94 eV) is the most luminous line. More
 446 generally, NGC 7319 shows overall higher luminosity in
 447 all lines compared to Sombrero and NGC 1052, with the
 448 relative luminosity increasing for the higher IP lines.

449 The middle panel of Figure 3 shows the $\text{FWHM}_{\text{line}}$
 450 (see equation 1) of each line as a function of IP. These
 451 $\text{FWHM}_{\text{line}}$ values are derived from the best-fit multi-
 452 Gaussian model to the nuclear emission lines (Sec-
 453 tion 3.2.1). The red and blue dashed lines represent
 454 arcsecond-level central velocity dispersions for Sombrero
 455 and NGC 1052 ([Ho et al. 2009](#)) translated to a FWHM.
 456 The emission lines in Sombrero and NGC 1052 are
 457 visibly broader than those in NGC 7319 (as can be
 458 seen in Figure 1). Specifically, in NGC 7319 the lines
 459 have $\text{FWHM}_{\text{line}} \sim 200 \text{ km s}^{-1}$ regardless of IP. Mean-
 460 while in Sombrero and NGC 1052, all detected lines
 461 are significantly wider, with the broadest lines having
 462 $\text{FWHM}_{\text{line}} \gtrsim 1000 \text{ km s}^{-1}$. A clear trend is also seen with
 463 IP in Sombrero with the higher IP lines having signifi-
 464 cantly larger $\text{FWHM}_{\text{line}}$ values. A similar trend is seen
 465 in NGC 1052 though with the [Ne VI] $\lambda 7.65 \mu\text{m}$ emission
 466 feature being notably narrower than other high-IP lines.
 467 A similar correlation is found between FWHM and IP
 468 in NGC 7469 ([Armus et al. 2023](#)) when comparing the
 469 FWHM of the broad components of the emission lines.
 470 The widths of these components range from approxi-
 471 mately 600 km s^{-1} to 1100 km s^{-1} , falling between the
 472 ranges seen in NGC 7319 and Sombrero.

473 Finally, the bottom panel of Figure 3 shows the
 474 peak velocity of the emission lines as a function of IP.

475 The peak velocity is measured from our best-fit multi-
 476 Gaussian models and we see distinct differences between
 477 the galaxies here. For NGC 7319, the peak velocities are
 478 quite close to zero at all IP, which some slightly blue-
 479 shifted lines ($\sim 50 \text{ km s}^{-1}$) at intermediate IPs. The
 480 exception is the [O IV] line, which shows a significant
 481 blue-shift. We caution that this line is one of the longest
 482 wavelength lines we have; the wavelength calibration is
 483 less accurate at long wavelengths, but is still estimated
 484 to be $< 30 \text{ km s}^{-1}$ by [Argyriou et al. \(2023\)](#); this line is
 485 also among the most blue-shifted lines in Sombrero and
 486 NGC 1052.

487 For Sombrero, the high-IP lines are almost all signifi-
 488 cantly blueshifted (greater than 3σ from zero), while
 489 the lower IP lines and H_2 lines show a slight redshift.
 490 The redshift of the H_2 lines in Sombrero (median Peak
 491 Velocity of 56 km s^{-1}) may indicate that our systemic
 492 velocity taken from HI measurements ([de Vaucouleurs](#)
 493 [et al. 1991](#)) is offset; if this were the case most of the
 494 low- and mid-IP lines would show a modest blue-shift
 495 with a general trend of larger blue-shift with higher IP.
 496 In NGC 1052, the blueshift in the highest IP lines are
 497 weaker, but there is also a sign of blue-shifted emission
 498 even at lower IP. The blue-shifted emission could be due
 499 to outflows, which we discuss in detail in Section 5.3.

500 4.1.2. Detailed Nuclear Line Profiles

501 The high spectral resolution of JWST lets us resolve
 502 line widths and look at the detailed shapes of emission
 503 lines. Above we found that the high-IP lines show broad,
 504 often blue-shifted emission lines, and here we look in
 505 more detail at the shapes of the lines with the highest
 506 signal-to-noise ratios ($\text{S/N} > 50$). Figure 4 shows these
 507 lines in each galaxy centered on their expected veloc-
 508 ity. Looking at each galaxy, these strong lines show
 509 remarkably consistent line profiles suggesting a com-
 510 mon physical origin. However, significant differences
 511 are seen between galaxies, with Sombrero having a no-
 512 tably asymmetric line profile with blue wings reaching
 513 $> 1000 \text{ km s}^{-1}$, while NGC 1052 and NGC 7319 show
 514 more symmetric lines. The strong asymmetry in Som-
 515 brero likely indicates the presence of an outflow, which
 516 we will discuss in more detail in Section 5.3. Blue asym-
 517 metries are also observed in the highest IP emission line
 518 profiles of NGC 7469 ([Armus et al. 2023](#)). The narrower
 519 lines in NGC 7319 relative to the other two galaxies are
 520 clearly visible as well. We note that the highest IP lines
 521 in NGC 1052 and Sombrero are not high enough S/N to
 522 examine their line profiles in detail (as well as blending
 523 issues in a couple lines).

524 4.2. 2-D Emission Line Information: Line Maps & 525 FWHM

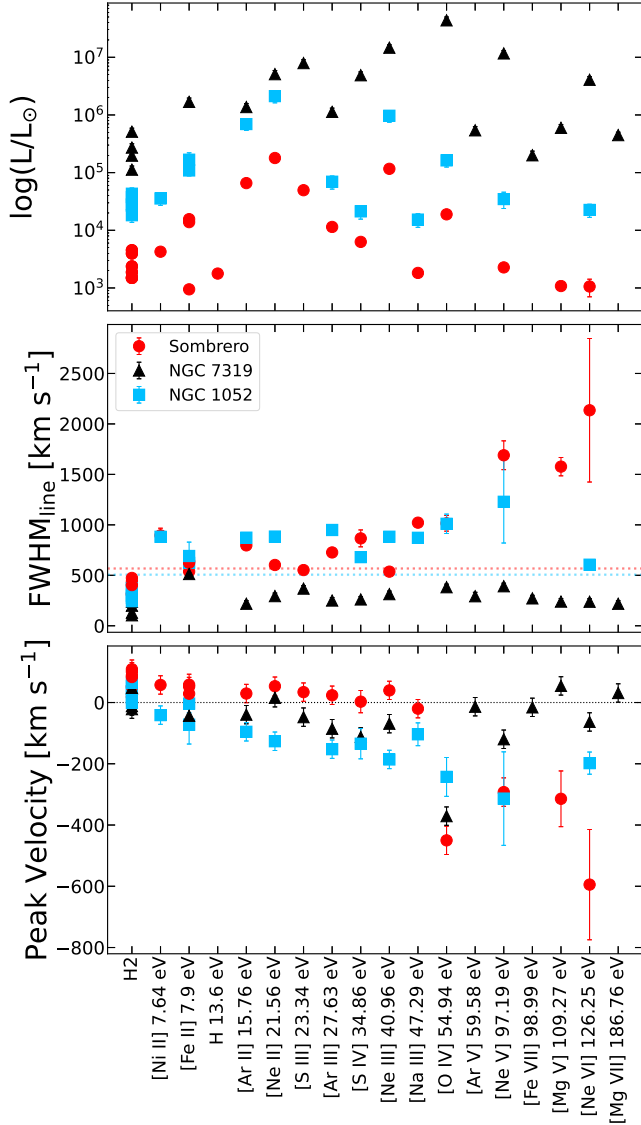


Figure 3. Emission-line trends with ionization potential. Emission features are listed along the x-axis ordered by their IP. *Top* – *Luminosity vs IP*. Emission-line luminosities scale with the Eddington ratio of sources. NGC 7319 has the highest Eddington ratio and the most luminous emission lines, followed by NGC 1052, and then Sombrero. The luminosities have a median fractional error of 15%. *Middle* – *FWHM_{line} vs IP*. The FWHM_{line} of emission features increases with IP in Sombrero and NGC 1052 while the FWHM_{line} of NGC 7319 emission features stays relatively constant with IP. FWHM_{line} in km s⁻¹ is shown on the y-axis with a median error of 30 km s⁻¹. Red and blue dashed lines represent the central stellar velocity dispersion measurements from Ho et al. (2009) translated to a FWHM. *Bottom* – *Peak Velocity vs IP*. Peak velocity of emission lines trend increasingly blue-shifted with increasing ionization potential in Sombrero and NGC 1052. The y-axis shows the peak velocity of the best fit Gaussian model with a median error of 30 km s⁻¹.

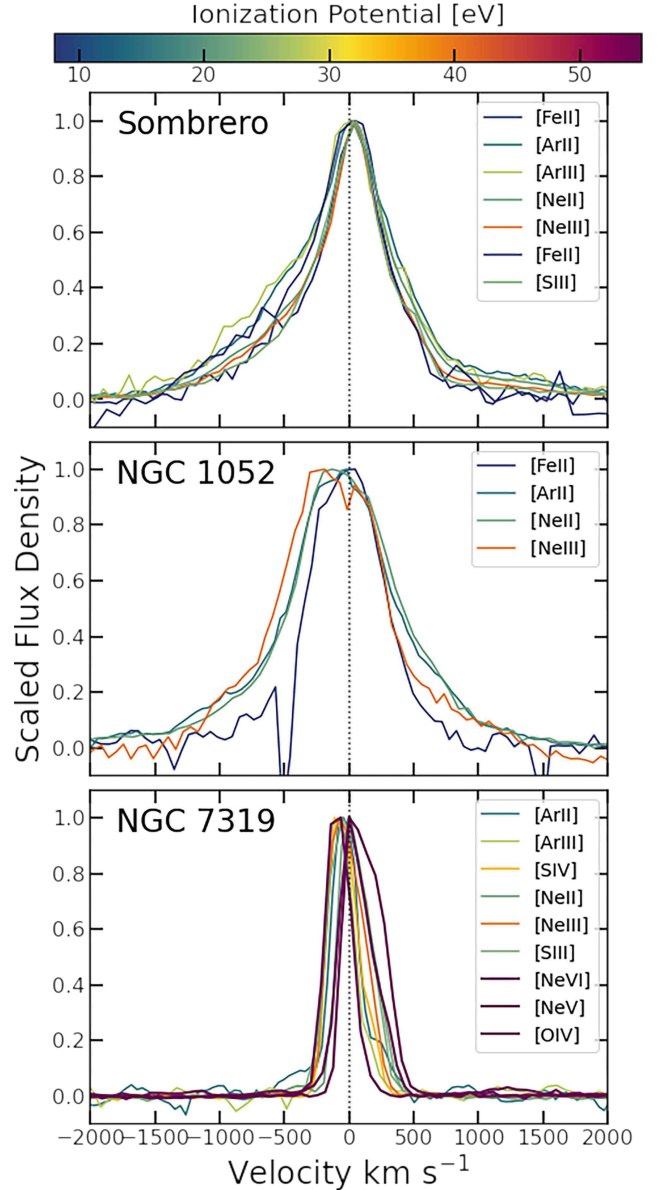


Figure 4. Nuclear emission-line profiles with S/N > 50 centered on expected velocity. Sombrero lines are asymmetrical with a blueshifted extension, or wing, while NGC 1052 and NGC 7319 have generally more symmetric profiles with blue-shifted peaks. Emission lines in NGC 7319 show red-shifted extensions at high IP.

526

4.2.1. Flux and Velocity Maps

527 Figure 5 shows flux and velocity maps for three lines
 528 in both Sombrero and NGC 1052. These are created
 529 using the single Gaussian fitting method described in
 530 Section 3.2.2. Three lines are shown for each galaxy;
 531 The H₂ 0–0 S(3) line at 9.66 μm, the [Ar II] line at 6.98
 532 μm (IP: 15.76 eV), and the [Ne III] line at 15.56 μm (IP:
 533 40.96 eV). These three lines span a wide range of IP and

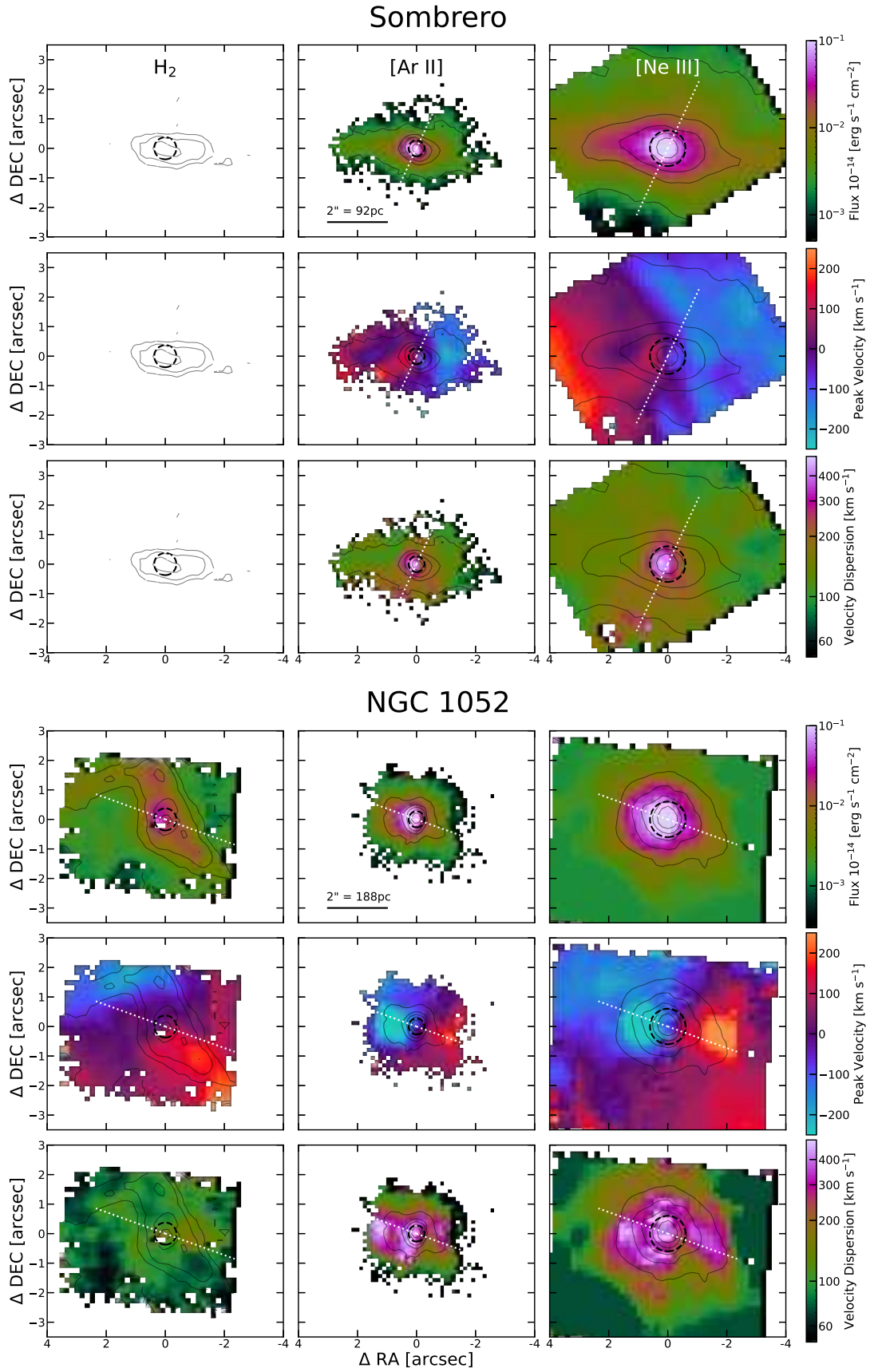


Figure 5. Flux, velocity, and dispersion maps for three emission lines in both Sombrero and NGC 1052. In all maps north is up and east is to the left. The leftmost column shows the $\text{H}_2(0-0)\text{S}(3)$ molecular hydrogen line at $9.66\ \mu\text{m}$, the middle column shows the low-IP line $[\text{Ar II}]\lambda 6.98\ \mu\text{m}$, and the right column shows the mid-IP line $[\text{Ne III}]\lambda 15.56\ \mu\text{m}$. Contours indicate flux levels of 1, 5, 10, 25, and 50% of the peak line flux, while the dashed black line represents the aperture used to extract the nuclear spectrum at that wavelength. The white dotted lines, (shown with arbitrary length) indicate the orientation of compact radio jets; corresponding to a PA of -25° in Sombrero oriented nearly along our line-of-sight (Hada et al. 2013), and a PA of 70° in NGC 1052 oriented along the plane of the sky (Kadler et al. 2004b).

critical densities and thus likely trace very different density gas (e.g. Stern et al. 2014). The highest IP lines (IP > 50 eV) are unresolved, and therefore compact, showing detectable emission only in the central few pixels.

In the Sombrero galaxy, all three lines have similar morphologies, extended east-to-west with blue-shifted emission towards the west. The molecular hydrogen emission has no clear point-like emission and is red-shifted relative to the systemic velocity in the nuclear region; this redshift is also seen in several other H_2 and low IP lines in Sombrero (Figure 3). As discussed in the previous subsection, this may be due to the adopted systemic velocity for Sombrero. The velocity dispersion seen in molecular hydrogen emission maps is quite homogeneous with values up to 240 km s^{-1} , comparable to the measured nuclear stellar velocity dispersion (241 km s^{-1} ; Ho et al. 2009). Clear point-like emission is seen in both $[\text{Ar II}] \lambda 6.98 \mu\text{m}$ and $[\text{Ne III}] \lambda 15.56 \mu\text{m}$; this emission appears to be more concentrated in $[\text{Ar II}] \lambda 6.98 \mu\text{m}$ than $[\text{Ne III}] \lambda 15.56 \mu\text{m}$, however this may be due simply to the lower resolution at these wavelengths; we examine this in more detail below in Section 4.2.2. Filaments can be seen extending out to the north/west from the nuclear region in the $[\text{Ne III}] \lambda 15.56 \mu\text{m}$ flux map. The velocity maps of both ions shown are similar to H_2 (red-shifted to the east, and blue-shifted to the west), but show complex velocity fields e.g. a patch of blue-shifted emission $\sim 2''$ east of the nucleus and a stretch of red-shifted emission stretching south-east from the nuclear region. The velocity dispersion in $[\text{Ar II}] \lambda 6.98 \mu\text{m}$ and $[\text{Ne III}] \lambda 15.56 \mu\text{m}$ both peak in the nuclear region with a maximum velocity of about 500 km s^{-1} .

In NGC 1052, the H_2 emission-line map differs significantly from the $[\text{Ar II}] \lambda 6.98 \mu\text{m}$ and $[\text{Ne III}] \lambda 15.56 \mu\text{m}$ emission. The H_2 emission-line flux maps have a weak peak in the nuclear region and extend north-east to south-west. The velocity maps of H_2 are blue-shifted in the north-east and red-shifted to the south and west. The velocity dispersion is larger along the minor axis of rotation and peaks at $\sim 275 \text{ km s}^{-1}$ in the nuclear region, a bit higher than the Ho et al. (2009) central stellar velocity dispersion of 215 km s^{-1} . The H_2 flux, velocity, and dispersion maps presented here for NGC 1052 are in agreement with Müller-Sánchez et al. (2013) where the H_2 1-0 S(1) line at $2.12 \mu\text{m}$ was examined using SINFONI, benefiting from slightly better spatial resolution. Müller-Sánchez et al. (2013) interpret the morphology and kinematics of H_2 as a decoupled rotating disk, due to the gas having a kinematic major axis that is not aligned with the stellar rotation axis. Our H_2 flux map is also similar in morphol-

ogy to the CO gas seen with ALMA in (Kameno et al. 2020), which they interpret as a circumnuclear disk. The $[\text{Ar II}] \lambda 6.98 \mu\text{m}$ and $[\text{Ne III}] \lambda 15.56 \mu\text{m}$ emission-line flux maps are strongly peaked in the nucleus and share a roughly concentric radial profile. The corresponding velocity maps of NGC 1052 reveal extended emission with a distinct kinematic structure characterized by a heavily blue-shifted region directly East of the nucleus and a heavily red-shifted region to the West, with velocities up to 590 km s^{-1} . As detailed in Section 1, NGC 1052 has an inner radio jet on $\sim 2 \text{ pc}$ scales with a PA of ~ 70 degrees (Claussen et al. 1998; Kadler et al. 2004b), while at larger scales ($\sim 1 \text{ kpc}$) the PA of the radio jets is approximately 100 degrees (Wrobel 1984; Kadler et al. 2004a). Our MIRI/MRS data falls between these two scales, and the PA of the kinematic structure we see (Figure 5) falls between the PAs of these inner and outer jets.

4.2.2. Spatial FWHM Measurements

Following the methodology outlined in Section 4.2.1, we determine $\text{FWHM}_{\text{spat,corr}}$, characterizing the PSF-corrected spatial extent, for six emission lines in Sombrero and four emission lines in NGC 1052. These lines are at low- and mid- IP and have sufficient signal-to-noise to enable the measurement. The FWHM_{MRS} , $\text{FWHM}_{\text{spat}}$ and $\text{FWHM}_{\text{spat,corr}}$ measurements are provided in Table 3. Overall, we find that the lines in NGC 1052 are either unresolved or just barely spatially resolved, with the $[\text{Ne III}]$ line having the largest spatial extent ($\text{FWHM}_{\text{spat,corr}} = 0''.30$ or 28.2 pc). On the other hand, all the emission lines in Sombrero are spatially resolved, with $\text{FWHM}_{\text{spat,corr}} > 0''.17$ or 8 pc , and no clear trend with IP. We note that while $\text{FWHM}_{\text{spat,corr}}$ estimates were not possible for the high-IP coronal lines ($[\text{O IV}] \lambda 25.91 \mu\text{m}$ and $[\text{Ne V}] \lambda 14.32 \mu\text{m}$), these lines do appear to be quite compact in both galaxies. In both galaxies, the $[\text{Ne III}] \lambda 15.56 \mu\text{m}$ emission is more extended than the $[\text{Ne II}] \lambda 12.81 \mu\text{m}$ emission, a somewhat surprising result that we discuss further in Section 5.2.

5. DISCUSSION

In this section we present our results in the context of previous work. First, in section 5.1, we discuss the power of JWST in separating LLAGN from their host galaxies. Then in section 5.2, we compare the nuclear emission features from our LLAGN to AGNs of varying types, and end with section 5.3 by discussing evidence for outflows seen in the LLAGN spectra.

5.1. The Promise of JWST for Revealing LLAGN

In Figure 6 we show a comparison of the extracted nuclear spectrum (see Section 3.1) in Sombrero to both

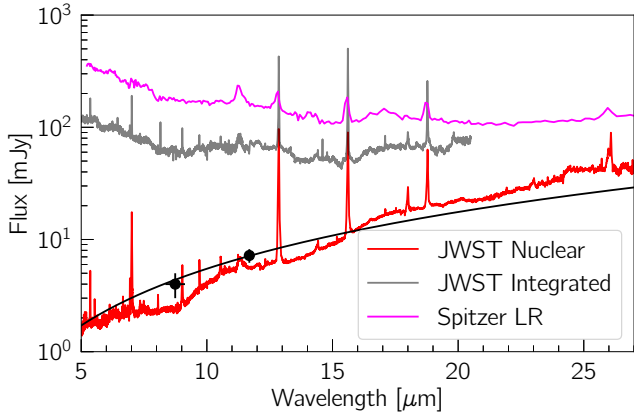


Figure 6. JWST enables us to separate LLAGN spectra from their host galaxy. Comparison of the aperture corrected nuclear extracted spectrum in Sombrero (red line; same as Figure 1), to the integrated MIRI/MRS spectrum (gray line; FoV: $6''.6 \times 7''.7$), and the Spitzer LR spectrum (magenta line; FoV: $27''.7 \times 51''.8$). The black line shows the best fit high-spatial resolution power-law fit to Sombrero from Fernández-Ontiveros et al. (2023) this is fit to the black points, which are photometry from Gemini (Asmus et al. 2014) and VLT (Fernández-Ontiveros et al. 2023) as well as sub-arcsecond data at shorter wavelengths; both the data and fit are in good agreement with our nuclear spectrum. We show the integrated spectrum only out to $20 \mu\text{m}$ as the poorly constrained MIRI channel 4 background levels significantly impact the integrated spectrum measurements at redder wavelengths.

the integrated flux in the JWST data cube, and the Spitzer LR spectrum from the SINGS survey (Kennicutt et al. 2003). The integrated flux was calculated by summing all spaxels in each MIRI data cube. Since the FoV varies between each channel, we normalized the integrated spectrum to channel 4. In this channel the FoV measures $6''.6 \times 7''.7$ corresponding to a physical scale of $306 \times 357 \text{ pc}^2$ at the distance of Sombrero. Note that the integrated spectrum is not shown at the longest wavelengths due to sky subtraction issues as discussed in Gasman et al. (2023).

The nuclear emission clearly shows a SED that increases with wavelength, while the integrated data cube has a very different SED. Just $\sim 1\%$ of the flux in the JWST integrated cube is coming from the nuclear component at $5 \mu\text{m}$, while the nuclear component is $>10\%$ of the flux by $20 \mu\text{m}$. This rising nuclear SED is consistent with two previous photometric measurements of Sombrero at high resolution (black points/line in Figure 6) and within the expectations of LLAGN spectra (Fernández-Ontiveros et al. 2023). However, the information available in the nuclear spectrum is clearly far richer than was available with previous ground-based photometric measurements.

The two larger scale spectra from both Spitzer and our integrated JWST data in Figure 6 show very different spectral shapes that are dominated by galaxy emission. The shape of these two spectra are in good agreement despite the different apertures suggesting a roughly constant SED for the galaxy component. Overall, the data show that even in Sombrero, the faintest target in the ReveaLLAGN survey, we can cleanly extract the LLAGN emission and separate it from its surrounding galaxy. Although the primary goal of this paper is analysis of the emission lines in our ReveaLLAGN MIRI spectra, the continuum shape also encodes information on the emission mechanisms of these LLAGN. High angular resolution work on LLAGN has consistently shown jet dominated emission to follow a broken power-law continuum (Ho et al. 1996; Chary et al. 2000; Prieto et al. 2016; Fernández-Ontiveros et al. 2023) which is consistent with self-absorbed synchrotron emission characteristic of compact jet emission (Marscher & Gear 1985).

While Figure 6 shows broad agreement with a single power-law fit from Fernández-Ontiveros et al. (2023) over the MIRI wavelength range, there is also considerable complexity seen in the SEDs (Figure 1), with a clear inflection point in the Sombrero nuclear spectrum at $9 \mu\text{m}$. We also see a gradual flattening of the spectrum at long wavelengths in NGC 1052, which is consistent with the turnover of the broken power below $20 \mu\text{m}$ and the nuclear fluxes at lower frequencies (Fernández-Ontiveros et al. 2019). The complexity of the continuum shapes we see in the MIRI spectra suggest additional information may be available from detailed fitting of the continuum that includes the contributions of broad silicate features (Fernández-Ontiveros et al., *in prep*).

5.2. The Emission Lines of LLAGN: Comparison to Previous Work

In this subsection, we focus on comparing the nuclear emission-line luminosities and ratios to previous measurements of typically much higher luminosity AGN.

Figure 7 compares the luminosities of the two high-IP lines detected in all three galaxies, $[\text{Ne V}] \lambda 14.32 \mu\text{m}$ and $[\text{O IV}] \lambda 25.91 \mu\text{m}$ to literature measurements primarily from Spitzer (Goulding & Alexander 2009; Tommasini et al. 2010; Fernández-Ontiveros et al. 2016). We note that these data have much lower physical resolution than our nuclear JWST data, and thus contamination of the AGN spectra by galaxy light is likely significant in some cases, especially for lower-IP lines discussed below that are excited by sources other than the AGN. NGC 7319 and NGC 7469, as expected, have luminosities very typical of previously measured AGN, while Sombrero has the

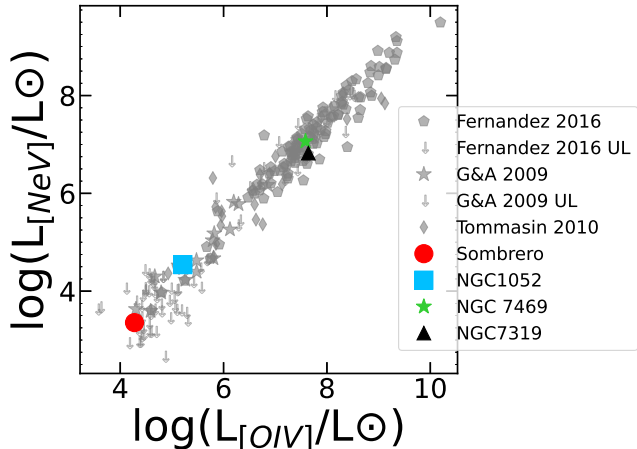


Figure 7. Sombrero and NGC 1052 have very low luminosity detections of [Ne V] $\lambda 14.32 \mu\text{m}$ and [O IV] $\lambda 25.91 \mu\text{m}$, with [Ne V] $\lambda 14.32 \mu\text{m}$ in Sombrero having one of the lowest luminosity detections to date. A tight, nearly linear relationship can be seen when comparing the luminosities of coronal lines [O IV] $\lambda 25.91 \mu\text{m}$ (x-axis) and [Ne V] $\lambda 14.32 \mu\text{m}$ (y-axis). The logarithm of the luminosity on both axes is shown in solar units ($3.846 \times 10^{33} \text{erg s}^{-1}$). Gray markers represent results from previous surveys (Goulding & Alexander 2009; Tommasin et al. 2010; Fernández-Ontiveros et al. 2016) with upper limits on [Ne V] found in Goulding & Alexander (2009) and Fernández-Ontiveros et al. (2016). The green star represents measurements for NGC 7469 taken from Armus et al. (2023)

lowest luminosities of both lines compared to any previous measurements. While Sombrero and NGC 1052 stand out as being very low luminosity detections, they both follow the tight, nearly linear correlation between these two coronal lines that is seen across a wide range of AGNs (Goulding & Alexander 2009).

Comparing ionized states of a particular atom enables us to study the ionization structure within an AGN more clearly. In this regard, the mid-IR is particularly valuable as it contains multiple neon emission lines at different ionizations. In Figure 8 we compare the flux values of [Ne II] $\lambda 12.81 \mu\text{m}$, [Ne III] $\lambda 15.56 \mu\text{m}$, and [Ne V] $\lambda 14.32 \mu\text{m}$ from our sample to previous surveys. Comparing line fluxes (rather than luminosities) ensures that correlations seen are the result of excitation differences, and not caused by observing sources at a range of distances (which can create false correlations between line luminosities).

The left panel comparing [Ne V]⁶ and [Ne III] shows a roughly linear correlation that gets tighter with in-

⁶ For the rest of the discussion, we will refer to [Ne II] $\lambda 12.81 \mu\text{m}$, [Ne III] $\lambda 15.56 \mu\text{m}$ and [Ne V] $\lambda 14.32 \mu\text{m}$ as [Ne II], [Ne III] and [Ne V], respectively.

creasing [Ne V] flux. Sombrero has significantly weaker [Ne V] than other sources with similar [Ne III] flux, and many of the lower luminosity sources including NGC 1052 also scatter towards fainter [Ne V] flux relative to the relation seen at higher line fluxes. Thus Sombrero is an outlier, but follows the qualitative trend of lower [Ne V] luminosity that are seen in other lower luminosity AGN. The middle panel comparing the flux of [Ne II] to [Ne V] shows similar results to the left panel, but with a much looser relation seen between the lines at high line fluxes. Finally the right panel shows that the relative [Ne II] and [Ne III] flux fall within the range of previous measurements in all three galaxies. This suggests that these lower IP lines have values typical of higher luminosity AGN, and it is the [Ne V] line that is weaker than in other sources.

We combine the information on all three neon lines in Figure 9, which compares the ratios of [Ne V]/[Ne II] and [Ne III]/[Ne II]. The ratio of [Ne V] to [Ne II] has been employed as a diagnostic tool in IR spectra to assess the contribution of AGN activity (Goulding & Alexander 2009; Sajina et al. 2022). Since [Ne V] can only be formed through AGN processes, while [Ne II] can arise from both AGN and non-AGN mechanisms, this ratio helps determine the presence and influence of AGN. We emphasize again, that the literature data here have low spatial resolution, and therefore any line emission in the central kiloparsecs of the galaxies contain significant contamination from the host galaxy. NGC 1052 and especially Sombrero fall well below the main trend line found in Figure 9 and into a region only populated with upper limits of [Ne V] from other surveys.

We can get a sense of the level of galaxy contamination in our own JWST spectra by comparing the extent of emission features with different IP and in Section 4.2.2 we find that the $\text{FWHM}_{\text{spat,corr}}$ of the [Ne II] and [Ne III] emission lines are quite compact. We would expect [Ne II] be more spatially extended than higher IP lines, including [Ne III], since [Ne II] lines come predominantly from star formation. This is not what we find in either source; in fact [Ne II] is found to be more compact than [Ne III] in both NGC 1052 and Sombrero. The fact that [Ne II] emission is compact doesn't strictly mean that it comes from the AGN, it could simply mean that any star formation is also compact/unresolved. While Prieto et al. (2014) reports the presence of extended H α emission perpendicular to the jet in Sombrero, which may be associated with star formation, they find no conclusive evidence of star formation, from UV to IR, within parsecs of the center of Sombrero, nor in NGC 1052 (Prieto et al. 2021). A lack of excitation from star formation is consistent with the absence of any PAH emission in

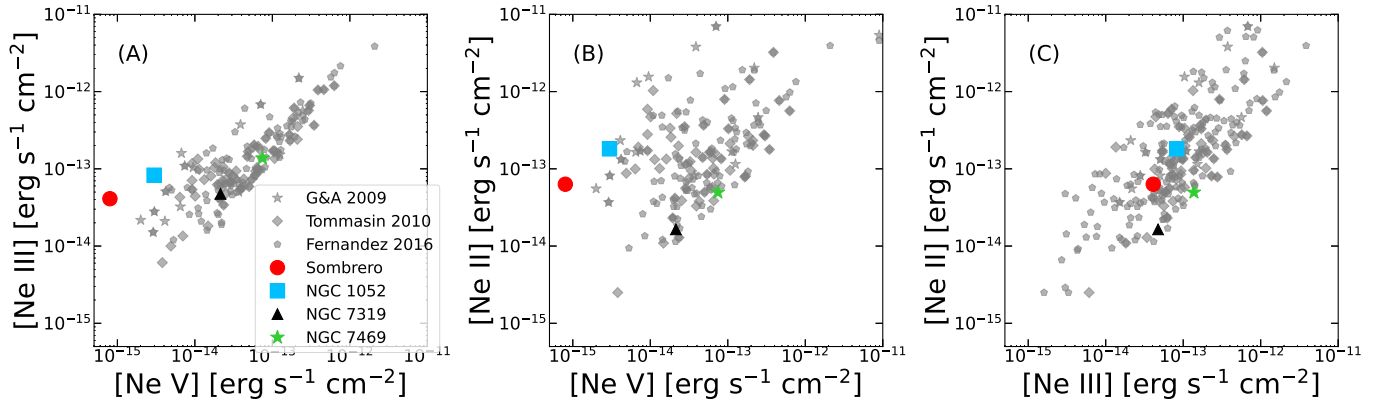


Figure 8. Flux measurements of different ionized states of neon from our sample compared to previous AGN surveys. The [Ne V] $\lambda 14.32 \mu\text{m}$ flux from our sample, especially in Sombrero, is much lower than in previously observed AGN relative to the [Ne III] $\lambda 15.56 \mu\text{m}$ (Plot A) and [Ne II] $\lambda 12.81 \mu\text{m}$ (Plot B) fluxes. However, the [Ne II] and [Ne III] fluxes are fairly typical of other AGN (plot C). Units on all axes are in $\text{erg s}^{-1} \text{cm}^{-2}$. Markers are the same as in 7.

782 the nuclear spectra of NGC 1052 and only a weak PAH
 783 signature at $11.3 \mu\text{m}$ in Sombrero (Fig. 1). This lack
 784 of evidence for star formation suggests that the nuclear
 785 line ratios from our targets (Figure 9) are not signifi-
 786 cantly contaminated by emission from star formation,
 787 and that the outlier status of our two galaxies are the
 788 result of very low luminosity detections of [Ne V] made
 789 possible by the spatial and spectral resolution of JWST.
 790 The differences we see then in Figure 8 are due to ex-
 791 citation differences from the AGN accretion structure.
 792 This difference can be explained by either a change in
 793 SED or very low ionization parameters that result in a
 794 deficiency of the high energy photons ($\gtrsim 100 \text{ eV}$) needed
 795 to excite the line. This conclusion is consistent with
 796 previous work on LLAGNs (Ho 2008; Eracleous et al.
 797 2010) including photoionisation models for compact jet
 798 synchrotron emission (Fernández-Ontiveros et al. 2023),
 799 shock excitation models (Dopita et al. 2015), and the
 800 expectations of a central engine with advection domi-
 801 nated accretion flows (Nemmen et al. 2014). We will be
 802 able to test this result and compare this to models for
 803 AGN ionization once the full ReveaLLAGN sample is
 804 available (Fernández-Ontiveros et al., *in prep*).

805 5.3. Outflows in NGC 1052 and Sombrero

806 In Section 4.1, we identify the following emission-line
 807 features in NGC 1052 and Sombrero:

- 808 • an increase in line widths with IP
- 809 • an increase in blue-shifted emission with IP
- 810 • broad emission in the weakly-detected high-IP and
 811 coronal lines, and
- 812 • prominent blue wings in the high signal-to-noise
 813 lines of Sombrero.

814 The trend of increasing line width and IP was origi-
 815 nally attributed to cloud stratification—the coronal lines

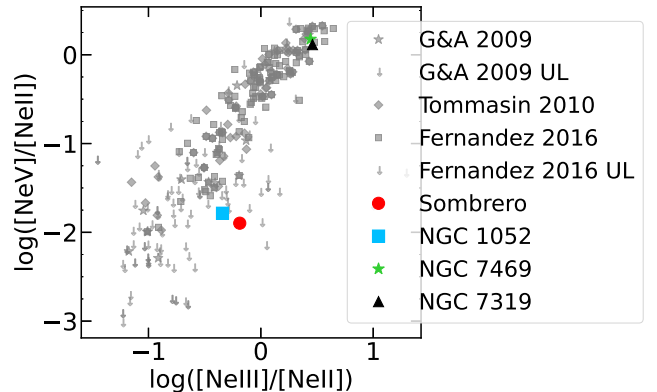


Figure 9. The low-luminosity detections of [Ne V] place our LLAGN sample well below the trend line when comparing the logarithm of [Ne III] $\lambda 15.56 \mu\text{m}$ /[Ne II] $\lambda 12.81 \mu\text{m}$ (x-axis) to the logarithm of [Ne V] $\lambda 14.32 \mu\text{m}$ /[Ne II] $\lambda 12.81 \mu\text{m}$ (y-axis). Marker colors are the same as in Figure 7, and 8.

816 are emitted from denser clouds closer to the central en-
 817 gine which are subject to more intense ionizing flux (Fil-
 818 ippenko & Halpern 1984; Filippenko 1985; Filippenko
 819 & Sargent 1988; Appenzeller & Oestreich 1988). Re-
 820 cent work has confirmed that many Seyfert galaxies, re-
 821 gardless of brightness or AGN type, show an increase
 822 in both line FWHM and line blue-shifting with increas-
 823 ing IP (e.g., Rodríguez-Ardila et al. 2006, 2011; Armus
 824 et al. 2023). Furthermore, there are known correla-
 825 tions between blue-shifted emission and both increas-
 826 ing IP in coronal lines and increasing line width in the
 827 [O III] line in narrow-line Seyfert 1 galaxies (e.g. Ko-
 828 mossa et al. 2008). While there is clear evidence that
 829 coronal-line emission and their profiles are driven mainly
 830 by photoionization from the AGN (e.g., Nussbaumer &
 831 Osterbrock 1970; Korista & Ferland 1989; Oliva et al.
 832 1994; Pier & Voit 1995; Rodríguez-Ardila et al. 2011),

other work has demonstrated that outflows are needed to fully explain the observed emission (e.g., Appenzeller & Oestreich 1988; Erkens et al. 1997; Wilson & Raymond 1999; Rodríguez-Ardila et al. 2006, 2011; Müller-Sánchez et al. 2011). In fact, the blue-shifted emission even at mid-IPs could trace out-flowing material closer to the AGN than the narrower emission, with the line asymmetry being caused by red-shifted emission being absorbed along the line-of-sight (Komossa et al. 2008).

Given the known importance of outflows and shocked emission in LINERs (e.g., Ho 2008; Trump et al. 2011; Molina et al. 2018), we conclude that the emission-line features identified above are indicators of outflows for both Sombrero and NGC 1052. We discuss other evidence and the possible origins of the outflows in NGC 1052 and Sombrero below.

5.3.1. Previous Evidence of Outflows in NGC 1052

Previous work has demonstrated the presence of AGN-related outflows in NGC 1052 on multiple spatial scales. Optical IFS studies of NGC 1052 show evidence for an outflow from the AGN on larger scales (Sugai et al. 2005; Dopita et al. 2015; Dahmer-Hahn et al. 2019; Cazzoli et al. 2022). The outflow is roughly aligned with the radio jet (Claussen et al. 1998; Kadler et al. 2004b), with a PA of $\sim 70^\circ$ and is generally in good agreement with the velocity structures seen in Figure 5. These studies also find a broad $H\alpha$ and $H\beta$ component with a width of $\sim 3000 \text{ km s}^{-1}$; this is significantly broader than the widths of the mid and high-IP lines we see here.

Similarly, on much smaller spatial scales, Müller-Sánchez et al. (2013) finds evidence of outflows in the velocity dispersion maps of H_2 emission seen in the IR, while Pogge et al. (2000), Walsh et al. (2008) and Molina et al. (2018) found evidence for outflows in *HST* data. Both Pogge et al. (2000) and Walsh et al. (2008) found evidence for strong outflows as well as ionized regions associated with jet-like features. Meanwhile, Molina et al. (2018) demonstrated that shocked emission likely originating from these outflows are the dominant power source at just ~ 20 pc outside of the galaxy center. Similar to Dopita et al. (2015), Cazzoli et al. (2022) and this work, Molina et al. (2018) found that the shock-dominated, off-nuclear emission lines had widths consistent with $v \lesssim 500 \text{ km s}^{-1}$. They also found broad $H\alpha$ and $H\beta$ emission in the unresolved AGN spectrum, with FWHM $\sim 10^3 \text{ km s}^{-1}$. We note that a majority of the emission seen in Molina et al. (2018) lies within the JWST nuclear aperture used in this work.

5.3.2. Previous Evidence of Outflows in Sombrero

Given the low accretion rate and the presence of a small-scale radio jet, Sombrero likely has strong radio

outflows (Meier 2001; Fender & Belloni 2004). In fact, Walsh et al. (2008) determined that while Sombrero has organized motion within the central $0''.5$ consistent with an overall rotation pattern, there are significant irregularities that could be caused by outflows. Pogge et al. (2000) also found evidence of turbulent motion via spiral-like wisps in the narrow-band $H\alpha + [\text{N II}]$ imaging. Emsellem & Ferruit (2000) further identified a strong velocity gradient near the galaxy center, and noted that the kinematics of the gas within the central $1''$ was decoupled from the gas in the spiral wisps. These east-west oriented wisps are not well-aligned with the inner radio jet described by Hada et al. (2013) and Mezcuca & Prieto (2014), which runs along the north-south axis and is oriented towards our line of sight. We note that the presence of broad $H\alpha$ is unclear, with two analyses of the same HST spectra coming to different conclusions (Walsh et al. 2008; Hermosa Muñoz et al. 2020). Mason et al. (2015) found that the near-infrared SED appears to be similar to that of other type 2 LINERs, and Galimore et al. (2006) and Li et al. (2011) also found evidence for larger-scale outflows in Sombrero using radio and X-ray data, respectively.

5.3.3. Origins of Outflows

Here we consider two possible models for the outflows seen in NGC 1052 and Sombrero. We note that radiation pressure-driven outflows do not significantly contribute to the outflows seen in LLAGN (Meena et al. 2023), and therefore we do not discuss them below. As a reminder, both of these objects are classified as LINERs and exhibit low Eddington ratios (Table 1), with evidence of compact radio jets (Section 1; Section 4.2.1).

Winds Launched from the RIAFs:

Unlike traditional cold, thin-disk models, RIAFs occur when the accretion rate is sufficiently low that the inner disk puffs up and becomes a hot, advection-dominated accretion flow (Narayan & Yi 1995; Blandford & Begelman 1999; Yuan & Narayan 2014). Previous empirical studies showed that radio outflows from AGNs, including those with thin-disk accretion flows and RIAFs, increase in strength as the accretion rate decreases (e.g., Ho 2002; Meléndez et al. 2010). RIAFs extending to large scales can eliminate broad line emission (Elitzur & Ho 2009) and the “big blue bump” associated with thin-disk accretion (e.g., Trump et al. 2011); the corresponding lack of UV emission and broad line features in most LINER AGN (e.g., Nicastro et al. 2003; Ho 2008) suggests they may be powered by RIAFs.

The strong wind along the polar or jet direction in RIAFs that was predicted by magnetohydrodynamical numerical simulations (Yuan et al. 2012, 2015) has been ob-

935 servationally confirmed in recent years (e.g. Wang et al.
 936 2013; Cheung et al. 2016; Park et al. 2019; Shi et al.
 937 2021). These energetic winds originate in the coronal
 938 region of the accretion flow, implying that higher-IP
 939 lines would experience more intense outflows, and thus
 940 likely have larger widths, consistent with the findings
 941 presented in Section 4.1. Given their low accretion rates
 942 (see Table 1), the absence of the “big blue bump” in
 943 both of their SEDs (Fernández-Ontiveros et al. 2012),
 944 and the lack of clear broad H α emission in Sombrero
 945 (Walsh et al. 2008), it is likely that both NGC 1052
 946 and Sombrero are powered by a RIAF. Therefore, we
 947 conclude that the energetic winds driven by the hot ac-
 948 cretion flows in both LLAGNs likely contribute to the
 949 observed emission. However, we note that by their na-
 950 ture RIAFs do drive radio jets, and as such these winds
 951 may not be the sole explanation for the observed out-
 952 flows.

953 *Jet-Driven Outflows:*

954 Jets associated with AGN accretion are known to
 955 drive outflows that create shocked emission and can reg-
 956 ulate the star-formation rate in the galaxy (e.g., Silk &
 957 Rees 1998; Weinberger et al. 2017; Davé et al. 2019). In
 958 fact, while we did not find any trends with IP in the
 959 nuclear spectra of NGC 7319, Pereira-Santaella et al.
 960 (2022) found that high-IP coronal-line emission is de-
 961 tected close to the hot spots of the known radio jet,
 962 which they conclude indicates the presence of a jet-
 963 driven outflow.

964 Due to their less luminous, lower-accretion rate en-
 965 gines, the shocked emission driven by jets or outflows
 966 can often dominate over photoionization at small dis-
 967 tances from the nuclei in LLAGNs (Molina et al. 2018).
 968 Furthermore subparsec-scale radio jets occur more fre-
 969 quently in LINERs (Nagar et al. 2005), which could fur-
 970 ther indicate the presence of jet-driven outflows.

971 Recent work by Meenakshi et al. (2022) demonstrated
 972 that small-scale jets can produce large widths even in
 973 mid-IP lines like [O III] λ 5007, similar to the widths
 974 seen in our mid-IP lines studied here. They also con-
 975 clude that similar widths can be seen in the different
 976 gas phases of the ISM, which appears to be somewhat
 977 qualitatively true for NGC 1052—the observed positive
 978 correlation between IP and FWHM in NGC 1052 in Fig-
 979 ure 3 is much less pronounced than that in Sombrero.
 980 Furthermore, both Sugai et al. (2005) and Dopita et al.
 981 (2015) found evidence that the jet in NGC 1052 was
 982 interacting with the circumnuclear gas.

983 In both the RIAF- and jet-driven wind scenario, the
 984 orientation of the jet should impact the observable signa-
 985 tures. In Sombrero, modeling of VLBI data suggests the
 986 inner jet is oriented close to our line-of-sight (Hada et al.

987 2013), while in NGC 1052, the jet is oriented more in the
 988 plane of the sky (Kadler et al. 2004b). This difference
 989 in jet orientation may be the reason that only Sombrero
 990 shows the blue-shifted emission in its nuclear spectrum,
 991 while the ionized emission-line maps in NGC 1052 show
 992 strong strong blue- and red-shifts oriented close to the
 993 jet axis (Figure 5). However, since both RIAF- and jet-
 994 driven winds will result in an outflow in the jet direction,
 995 a combination of SED modeling on the smallest scales
 996 with emission-line analysis like that presented here is
 997 likely required to resolve what drives the outflows in
 998 LLAGN.

999 6. CONCLUSIONS

1000 This paper features the first observations of the Re-
 1001 veaLLAGN survey, a JWST project to characterize
 1002 seven nearby LLAGN. We present MIRI/MRS data of
 1003 the least and most luminous targets in our sample, Som-
 1004 brero and NGC 1052. We compare this data to that
 1005 of higher luminosity AGNs, specifically NGC 7319 and
 1006 NGC 4395. We characterize the numerous emission lines
 1007 seen in the nuclear spectrum and create line maps across
 1008 the MRS field of view for stronger lines.

1009 We find the following results:

- 1010 • The resolution and sensitivity of JWST allows us
 1011 to cleanly separate the AGN continuum and emis-
 1012 sion lines from the surrounding galaxy even in our
 1013 least luminous target, Sombrero.
- 1014 • The ionized emission lines in both Som-
 1015 brero and NGC 1052 are broad, and have
 1016 widths that increase with increasing IP reaching
 1017 FWHM > 1000 km s⁻¹. The highest IP lines (IP
 1018 > 50) show blue-shifted peak velocities with a me-
 1019 dian velocity of -423 km s⁻¹ seen in Sombrero
 1020 and -186 km s⁻¹ in NGC 1052.
- 1021 • The highest signal-to-noise ionic lines in Som-
 1022 brero with show a clear blue wing extending
 1023 > 1000 km s⁻¹ from the peak emission.
- 1024 • Sombrero has the lowest luminosity high-IP lines
 1025 ([O IV] and [Ne V]) yet detected in any source.
 1026 NGC 1052 also shows low luminosity in both these
 1027 lines, and the relative luminosity of these lines fol-
 1028 lows the relation seen in more luminous AGN.
- 1029 • The [Ne V] λ 14.32 μ m is weak relative to the
 1030 [Ne II] λ 12.81 μ m and [Ne III] λ 15.56 μ m as com-
 1031 pared to previously measured AGN. This does not
 1032 appear to be due to galaxy contamination, and
 1033 thus likely indicates a deficiency of high energy
 1034 ionizing photons in these LLAGN.

1035 Our full ReveaLLAGN dataset will include observa-
1036 tions of seven nearby LLAGN with both the NIRSpec
1037 IFU and MIRI/MRS. We will present the nuclear spec-
1038 tra of these in an upcoming paper (Seth et al., *in prep*),
1039 as well as an analysis of their emission lines (Goold et
1040 al. *in prep*). We will also be modeling the continuum
1041 emission and emission lines from the ReveaLLAGN sam-
1042 ple (Fernández-Ontiveros et al. *in prep*). The ReveaL-
1043 LAGN spectra will be valuable in both identifying the
1044 unique features of LLAGN, and revealing the nature of
1045 the central engine in LLAGN.

1046 We thank Ioannis Argyriou for his helpful suggestions
1047 and willingness to share data and the anonymous ref-
1048 erree for their useful comments that helped improve the
1049 paper. KG, AS, and DO acknowledge support from
1050 JWST Cycle 1 grant GO-2016. We acknowledge the
1051 ERO team for developing their observing program with
1052 a zero-exclusive-access period. The work of MM is sup-
1053 ported in part through a fellowship sponsored by the
1054 Willard L. Eccles Foundation. LCH was supported by
1055 the National Science Foundation of China (11721303,
1056 11991052, 12011540375, 12233001), the National Key
1057 R&D Program of China (2022YFF0503401), and the
1058 China Manned Space Project (CMS-CSST-2021-A04,
1059 CMS-CSST-2021-A06).

1060 *Facilities:* JWST (MIRI/MRS)

1061 *Software:* astropy (Astropy Collaboration et al.
1062 2018), lmfit (<https://github.com/lmfit/lmfit-py>),
1063 jwst calibration pipeline v1.8.2 ([https://github.com/](https://github.com/spacetelescope/jwst)
1064 [spacetelescope/jwst](https://github.com/spacetelescope/jwst))

Table 2. Nuclear Spectra Measurements

Galaxy	Line	Wavelength ^a	IP ^b	Transition	Flux	Flux Err	Peak Vel	Peak Vel Err	FWHM _{line}	FWHM _{line} Err	S/N	Warning
		μm	eV		$10^{-14}\text{erg s}^{-1}\text{cm}^{-2}$	$10^{-14}\text{erg s}^{-1}\text{cm}^{-2}$	km s^{-1}	km s^{-1}	km s^{-1}	km s^{-1}		
Sombrero	[Fe II]	5.340	7.90	$4F_{9/2}\text{-a } 6D_{9/2}$	0.488	0.004	50	30	540	30	94.5	0
Sombrero	H ₂	5.448	15.37	(12-10)O(9)	< 0.009	–	–	–	–	–	0.0	0
Sombrero	[Mg VII]	5.504	186.76	$3P_2\text{-}3P_1$	<0.020	–	–	–	–	–	1.7	0
Sombrero	H ₂	5.511	15.37	(0-0)S(7)	0.083	0.003	110	30	310	30	25.8	0
Sombrero	[Mg V]	5.608	109.27	$3P_1\text{-}3P_2$	0.038	0.004	-310	100	1580	110	7.9	0
Sombrero	H ₂	6.109	15.37	(0-0)S(6)	0.053	0.005	20	30	320	160	12.5	0
Sombrero	[Ni II]	6.636	7.64	$2D_{3/2}\text{-}2D_{5/2}$	0.150	0.004	60	30	900	80	35.2	0
Sombrero	[Fe II]	6.721	7.90	$4F_{9/2}\text{-a } 6D_{7/2}$	0.033	0.003	60	30	620	50	9.5	0
Sombrero	H ₂	6.909	15.37	(0-0)S(5)	0.159	0.003	100	30	400	30	49.9	0
Sombrero	[Ar II]	6.985	15.76	$2P_{1/2}\text{-}2P_{3/2}$	2.320	0.007	30	30	800	30	370.5	0
Sombrero	[Na III]	7.318	47.29	$2P_{1/2}\text{-}2P_{3/2}$	0.064	0.003	-20	30	1020	40	20.8	0
Sombrero	H	7.458	13.60	Pfund-alpha	0.063	0.003	130	30	1130	30	18.5	0
Sombrero	[Ne VI]	7.652	126.25	$2P_{3/2}\text{-}2P_{1/2}$	0.037	0.010	-590	170	2140	550	6.7	0
Sombrero	H ₂	8.026	15.37	(0-0)S(4)	0.053	0.001	50	30	440	30	32.7	0
Sombrero	[Ar III]	8.991	27.63	$3P_1\text{-}3P_2$	0.403	0.007	20	30	730	50	89.3	0
Sombrero	[Fe VII]	9.527	98.99	$3F_3\text{-}3F_2$	<2.195	–	–	–	–	–	0.1	0
Sombrero	H ₂	9.665	15.37	(0-0)S(3)	0.140	0.002	90	30	400	30	58.0	0
Sombrero	[S IV]	10.510	34.86	$2P_{3/2}\text{-}2P_{1/2}$	0.222	0.006	0	40	870	100	31.8	0
Sombrero	H ₂	12.278	15.37	(0-0)S(2)	0.042	0.002	60	30	530	40	16.6	1
Sombrero	H	12.367	13.60	Humph-alpha	0.050	0.004	-130	80	1670	190	15.7	1
Sombrero	[Ne II]	12.814	21.56	$2P_{1/2}\text{-}2P_{3/2}$	6.317	0.020	50	30	600	30	757.2	0
Sombrero	[Ar V]	13.102	59.58	$3P_1\text{-}3P_0$	<0.004	–	–	–	–	–	4.0	0
Sombrero	[Ne V]	14.322	97.19	$3P\text{-}3P_1$	0.080	0.004	-290	40	1690	140	32.7	0
Sombrero	[Cl II]	14.368	12.97	$3P_1\text{-}3P_2$	–	–	–	–	–	–	13.3	3
Sombrero	[Ne III]	15.555	40.96	$3P_1\text{-}3P_2$	4.101	0.015	40	30	540	30	556.2	0

NOTE—The complete table is presented in the online version of the *Astrophysical Journal*. Here we present the first few rows to show its form and content. The measured quantities provided here are derived from the multi-component Gaussian fits described in Section 3.2.1. We define the line as detected if the integrated flux of a best-fit single-Gaussian model has a $S/N \geq 5$; upper limits are provided for undetected emission lines. The “Warning” column identifies issues with the spectra (blended feature, bad pixel, etc). 0 – good fit; measurements reported. 1 – blended/possibly blended features based on visual inspection; measurements reported. 2 – unacceptable spectra quality; no measurements to report. 3 – no measurements to report due to deblending procedure (Section 3.2.1, Figure 2).

^aRest wavelengths from NIST.

^bIonization potential energy from NIST.

Table 3. Spatial FWHM Measurements of the Resolved Emission Lines

Feature	Rest Wavelength (μm)	IP eV	FWHM _{MRS} (arcsec)	Sombrero			NGC 1052		
				FWHM _{spat} (arcsec)	FWHM _{spat,corr} (arcsec)	(pc)	FWHM _{spat} (arcsec)	FWHM _{spat,corr} (arcsec)	(pc)
[Fe II]	5.34	7.9	0.27	0.49	0.42	19.45	0.36	0.24	22.34
[Ar II]	6.99	15.76	0.31	0.35	0.17	7.87	0.33	0.12	10.35
[Ar III]	8.99	27.63	0.42	0.46	0.20	9.26	0.41	– [‡]	–
[Ne II]	12.81	21.56	0.57	0.62	0.24	11.11	0.58	0.09	8.46
[Ne III]	15.56	40.96	0.63	0.70	0.31	14.35	0.69	0.30	28.22
[S III]	18.71	23.34	0.86	0.99	0.49	22.69	0.86	– [‡]	–

NOTE— The FWHM of the MRS PSF (FWHM_{MRS}) is taken from [Argyriou et al. \(2023\)](#). We combine this with the measured spatial FWHM (FWHM_{spat}) via Equation 2 to calculate the corrected FWHM (FWHM_{spat,corr}). We only report the lines that we were able to spatially resolve in at least one galaxy. See Section 4.2.2 for details.

* FWHM_{spat} measurement unavailable.

[‡] Line is unresolved, FWHM_{spat} < FWHM_{MRS}.

REFERENCES

- 1065 Appenzeller, I., & Oestreich, R. 1988, *AJ*, 95, 45,
1066 doi: [10.1086/114611](#)
- 1067 Argyriou, I., Glasse, A., Law, D. R., et al. 2023, *JWST*
1068 *MIRI flight performance: The Medium-Resolution*
1069 *Spectrometer*, doi: [10.48550/arXiv.2303.13469](#)
- 1070 Armus, L., Lai, T., U, V., et al. 2023, *ApJL*, 942, L37,
1071 doi: [10.3847/2041-8213/acac66](#)
- 1072 Asmus, D., Gandhi, P., Hönig, S. F., Smette, A., & Duschl,
1073 W. J. 2015, *MNRAS*, 454, 766,
1074 doi: [10.1093/mnras/stv1950](#)
- 1075 Asmus, D., Hoenig, S. F., Gandhi, P., Smette, A., &
1076 Duschl, W. J. 2014, *VizieR Online Data Catalog*,
1077 *J/MNRAS/439/1648*
- 1078 Astropy Collaboration, Price-Whelan, A. M., Sipőcz, B. M.,
1079 et al. 2018, *AJ*, 156, 123, doi: [10.3847/1538-3881/aabc4f](#)
- 1080 Blandford, R. D., & Begelman, M. C. 1999, *MNRAS*, 303,
1081 L1, doi: [10.1046/j.1365-8711.1999.02358.x](#)
- 1082 Bushouse, H., Eisenhamer, J., Dencheva, N., et al. 2022,
1083 *JWST Calibration Pipeline, 1.8.2*, Zenodo,
1084 doi: [10.5281/zenodo.7229890](#)
- 1085 Cazzoli, S., Hermosa Muñoz, L., Márquez, I., et al. 2022,
1086 *A&A*, 664, A135, doi: [10.1051/0004-6361/202142695](#)
- 1087 Chary, R., Becklin, E. E., Evans, A. S., et al. 2000, *ApJ*,
1088 531, 756, doi: [10.1086/308486](#)
- 1089 Cheung, E., Bundy, K., Cappellari, M., et al. 2016, *Nature*,
1090 533, 504, doi: [10.1038/nature18006](#)
- 1091 Claussen, M. J., Diamond, P. J., Braatz, J. A., Wilson,
1092 A. S., & Henkel, C. 1998, *ApJL*, 500, L129,
1093 doi: [10.1086/311405](#)
- 1094 Croton, D. J., Springel, V., White, S. D. M., et al. 2006,
1095 *MNRAS*, 365, 11, doi: [10.1111/j.1365-2966.2005.09675.x](#)
- 1096 Dahmer-Hahn, L. G., Riffel, R., Ricci, T. V., et al. 2019,
1097 *MNRAS*, 489, 5653, doi: [10.1093/mnras/stz2453](#)
- 1098 Davé, R., Anglés-Alcázar, D., Narayanan, D., et al. 2019,
1099 *MNRAS*, 486, 2827, doi: [10.1093/mnras/stz937](#)
- 1100 de Vaucouleurs, G., de Vaucouleurs, A., Corwin, Herold G.,
1101 J., et al. 1991, *Third Reference Catalogue of Bright*
1102 *Galaxies*
- 1103 Dopita, M. A., Ho, I. T., Dressel, L. L., et al. 2015, *ApJ*,
1104 801, 42, doi: [10.1088/0004-637X/801/1/42](#)
- 1105 Dudik, R. P., Satyapal, S., Gliozzi, M., & Sambruna, R. M.
1106 2005, *ApJ*, 620, 113, doi: [10.1086/426856](#)
- 1107 Elitzur, M., & Ho, L. C. 2009, *ApJL*, 701, L91,
1108 doi: [10.1088/0004-637X/701/2/L91](#)
- 1109 Elitzur, M., Ho, L. C., & Trump, J. R. 2014, *MNRAS*, 438,
1110 3340, doi: [10.1093/mnras/stt2445](#)
- 1111 Emsellem, E., & Ferruit, P. 2000, *A&A*, 357, 111,
1112 doi: [10.48550/arXiv.astro-ph/0003167](#)
- 1113 Eracleous, M., Hwang, J. A., & Flohic, H. M. L. G. 2010,
1114 *ApJS*, 187, 135, doi: [10.1088/0067-0049/187/1/135](#)
- 1115 Erkens, U., Appenzeller, I., & Wagner, S. 1997, *A&A*, 323,
1116 707
- 1117 Eskew, M., Zaritsky, D., & Meidt, S. 2012, *AJ*, 143, 139,
1118 doi: [10.1088/0004-6256/143/6/139](#)

- 1119 Fabbiano, G., & Juda, J. Z. 1997, *ApJ*, 476, 666,
1120 doi: [10.1086/303636](https://doi.org/10.1086/303636)
- 1121 Fender, R., & Belloni, T. 2004, *ARA&A*, 42, 317,
1122 doi: [10.1146/annurev.astro.42.053102.134031](https://doi.org/10.1146/annurev.astro.42.053102.134031)
- 1123 Fernández-Ontiveros, J. A., López-Gonzaga, N., Prieto,
1124 M. A., et al. 2019, *MNRAS*, 485, 5377,
1125 doi: [10.1093/mnras/stz716](https://doi.org/10.1093/mnras/stz716)
- 1126 Fernández-Ontiveros, J. A., López-López, X., & Prieto, A.
1127 2023, *A&A*, 670, A22, doi: [10.1051/0004-6361/202243547](https://doi.org/10.1051/0004-6361/202243547)
- 1128 Fernández-Ontiveros, J. A., Prieto, M. A., Acosta-Pulido,
1129 J. A., & Montes, M. 2012, in *Journal of Physics*
1130 *Conference Series*, Vol. 372, *Journal of Physics*
1131 *Conference Series*, 012006,
1132 doi: [10.1088/1742-6596/372/1/012006](https://doi.org/10.1088/1742-6596/372/1/012006)
- 1133 Fernández-Ontiveros, J. A., Spinoglio, L., Pereira-Santaella,
1134 M., et al. 2016, *ApJS*, 226, 19,
1135 doi: [10.3847/0067-0049/226/2/19](https://doi.org/10.3847/0067-0049/226/2/19)
- 1136 Filho, M. E., Barthel, P. D., & Ho, L. C. 2006, *A&A*, 451,
1137 71, doi: [10.1051/0004-6361:20054510](https://doi.org/10.1051/0004-6361:20054510)
- 1138 Filippenko, A. V. 1985, *ApJ*, 289, 475, doi: [10.1086/162909](https://doi.org/10.1086/162909)
- 1139 Filippenko, A. V., & Halpern, J. P. 1984, *ApJ*, 285, 458,
1140 doi: [10.1086/162521](https://doi.org/10.1086/162521)
- 1141 Filippenko, A. V., & Sargent, W. L. W. 1988, *ApJ*, 324,
1142 134, doi: [10.1086/165886](https://doi.org/10.1086/165886)
- 1143 Flohic, H. M. L. G., Eracleous, M., Chartas, G., Shields,
1144 J. C., & Moran, E. C. 2006, *ApJ*, 647, 140,
1145 doi: [10.1086/505296](https://doi.org/10.1086/505296)
- 1146 Fouque, P., Durand, N., Bottinelli, L., Gouguenheim, L., &
1147 Paturel, G. 1992, *Catalogue of Optical Radial Velocities*
1148 (*Observatoire de Lyon*)
- 1149 Gaia Collaboration, Brown, A. G. A., Vallenari, A., et al.
1150 2021, *A&A*, 649, A1, doi: [10.1051/0004-6361/202039657](https://doi.org/10.1051/0004-6361/202039657)
- 1151 Gallimore, J. F., Axon, D. J., O’Dea, C. P., Baum, S. A., &
1152 Pedlar, A. 2006, *AJ*, 132, 546, doi: [10.1086/504593](https://doi.org/10.1086/504593)
- 1153 Gasman, D., Argyriou, I., Sloan, G. C., et al. 2023, *A&A*,
1154 673, A102, doi: [10.1051/0004-6361/202245633](https://doi.org/10.1051/0004-6361/202245633)
- 1155 González-Martín, O., Masegosa, J., Márquez, I., &
1156 Guainazzi, M. 2009, *ApJ*, 704, 1570,
1157 doi: [10.1088/0004-637X/704/2/1570](https://doi.org/10.1088/0004-637X/704/2/1570)
- 1158 González-Martín, O., Masegosa, J., Márquez, I., Guerrero,
1159 M. A., & Dultzin-Hacyan, D. 2006, *A&A*, 460, 45,
1160 doi: [10.1051/0004-6361:20054756](https://doi.org/10.1051/0004-6361:20054756)
- 1161 Goulding, A. D., & Alexander, D. M. 2009, *MNRAS*, 398,
1162 1165, doi: [10.1111/j.1365-2966.2009.15194.x](https://doi.org/10.1111/j.1365-2966.2009.15194.x)
- 1163 Greene, J. E., Ho, L. C., & Ulvestad, J. S. 2006, *ApJ*, 636,
1164 56, doi: [10.1086/497905](https://doi.org/10.1086/497905)
- 1165 Guainazzi, M., & Antonelli, L. A. 1999, *MNRAS*, 304, L15,
1166 doi: [10.1046/j.1365-8711.1999.02470.x](https://doi.org/10.1046/j.1365-8711.1999.02470.x)
- 1167 Hada, K., Doi, A., Nagai, H., et al. 2013, *ApJ*, 779, 6,
1168 doi: [10.1088/0004-637X/779/1/6](https://doi.org/10.1088/0004-637X/779/1/6)
- 1169 Heckman, T. M. 1980, *A&A*, 87, 152
- 1170 Hermosa Muñoz, L., Cazzoli, S., Márquez, I., & Masegosa,
1171 J. 2020, *A&A*, 635, A50,
1172 doi: [10.1051/0004-6361/201936680](https://doi.org/10.1051/0004-6361/201936680)
- 1173 Hernández-García, L., González-Martín, O., Márquez, I., &
1174 Masegosa, J. 2013, *A&A*, 556, A47,
1175 doi: [10.1051/0004-6361/201321563](https://doi.org/10.1051/0004-6361/201321563)
- 1176 Hernández-García, L., González-Martín, O., Masegosa, J.,
1177 & Márquez, I. 2014, *A&A*, 569, A26,
1178 doi: [10.1051/0004-6361/201424140](https://doi.org/10.1051/0004-6361/201424140)
- 1179 Ho, L. C. 1999, *ApJ*, 516, 672, doi: [10.1086/307137](https://doi.org/10.1086/307137)
- 1180 —. 2002, *ApJ*, 564, 120, doi: [10.1086/324399](https://doi.org/10.1086/324399)
- 1181 —. 2008, *ARA&A*, 46, 475,
1182 doi: [10.1146/annurev.astro.45.051806.110546](https://doi.org/10.1146/annurev.astro.45.051806.110546)
- 1183 —. 2009, *ApJ*, 699, 626, doi: [10.1088/0004-637X/699/1/626](https://doi.org/10.1088/0004-637X/699/1/626)
- 1184 Ho, L. C., Filippenko, A. V., & Sargent, W. L. W. 1996,
1185 *ApJ*, 462, 183, doi: [10.1086/177140](https://doi.org/10.1086/177140)
- 1186 —. 1997, *ApJS*, 112, 315, doi: [10.1086/313041](https://doi.org/10.1086/313041)
- 1187 Ho, L. C., Greene, J. E., Filippenko, A. V., & Sargent, W.
1188 L. W. 2009, *ApJS*, 183, 1,
1189 doi: [10.1088/0067-0049/183/1/1](https://doi.org/10.1088/0067-0049/183/1/1)
- 1190 Jardel, J. R., Gebhardt, K., Shen, J., et al. 2011, *ApJ*, 739,
1191 21, doi: [10.1088/0004-637X/739/1/21](https://doi.org/10.1088/0004-637X/739/1/21)
- 1192 Kadler, M., Kerp, J., Ros, E., et al. 2004a, *A&A*, 420, 467,
1193 doi: [10.1051/0004-6361:20034126](https://doi.org/10.1051/0004-6361:20034126)
- 1194 Kadler, M., Ros, E., Lobanov, A. P., Falcke, H., & Zensus,
1195 J. A. 2004b, *A&A*, 426, 481,
1196 doi: [10.1051/0004-6361:20041051](https://doi.org/10.1051/0004-6361:20041051)
- 1197 Kameno, S., Sawada-Satoh, S., Impellizzeri, C. M. V., et al.
1198 2020, *ApJ*, 895, 73, doi: [10.3847/1538-4357/ab8bd6](https://doi.org/10.3847/1538-4357/ab8bd6)
- 1199 Kennicutt, Robert C., J., Armus, L., Bendo, G., et al. 2003,
1200 *PASP*, 115, 928, doi: [10.1086/376941](https://doi.org/10.1086/376941)
- 1201 Kewley, L. J., Groves, B., Kauffmann, G., & Heckman, T.
1202 2006, *MNRAS*, 372, 961,
1203 doi: [10.1111/j.1365-2966.2006.10859.x](https://doi.org/10.1111/j.1365-2966.2006.10859.x)
- 1204 Komossa, S., Xu, D., Zhou, H., Storchi-Bergmann, T., &
1205 Binette, L. 2008, *ApJ*, 680, 926, doi: [10.1086/587932](https://doi.org/10.1086/587932)
- 1206 Korista, K. T., & Ferland, G. J. 1989, *ApJ*, 343, 678,
1207 doi: [10.1086/167739](https://doi.org/10.1086/167739)
- 1208 Koss, M. J., Ricci, C., Trakhtenbrot, B., et al. 2022, *ApJS*,
1209 261, 2, doi: [10.3847/1538-4365/ac6c05](https://doi.org/10.3847/1538-4365/ac6c05)
- 1210 Lambert, S. B., & Gontier, A. M. 2009, *A&A*, 493, 317,
1211 doi: [10.1051/0004-6361:200810582](https://doi.org/10.1051/0004-6361:200810582)
- 1212 Li, Z., Jones, C., Forman, W. R., et al. 2011, *ApJ*, 730, 84,
1213 doi: [10.1088/0004-637X/730/2/84](https://doi.org/10.1088/0004-637X/730/2/84)
- 1214 Maoz, D., Nagar, N. M., Falcke, H., & Wilson, A. S. 2005,
1215 *ApJ*, 625, 699, doi: [10.1086/429795](https://doi.org/10.1086/429795)
- 1216 Marscher, A. P., & Gear, W. K. 1985, *ApJ*, 298, 114,
1217 doi: [10.1086/163592](https://doi.org/10.1086/163592)

- 1218 Mason, R. E., Rodríguez-Ardila, A., Martins, L., et al.
 1219 2015, *ApJS*, 217, 13, doi: [10.1088/0067-0049/217/1/13](https://doi.org/10.1088/0067-0049/217/1/13)
- 1220 McQuinn, K. B. W., Skillman, E. D., Dolphin, A. E., Berg,
 1221 D., & Kennicutt, R. 2016, *AJ*, 152, 144,
 1222 doi: [10.3847/0004-6256/152/5/144](https://doi.org/10.3847/0004-6256/152/5/144)
- 1223 Meena, B., Crenshaw, D. M., Schmitt, H. R., et al. 2023,
 1224 *ApJ*, 943, 98, doi: [10.3847/1538-4357/aca75f](https://doi.org/10.3847/1538-4357/aca75f)
- 1225 Meenakshi, M., Mukherjee, D., Wagner, A. Y., et al. 2022,
 1226 *MNRAS*, 516, 766, doi: [10.1093/mnras/stac2251](https://doi.org/10.1093/mnras/stac2251)
- 1227 Meier, D. L. 2001, *ApJL*, 548, L9, doi: [10.1086/318921](https://doi.org/10.1086/318921)
- 1228 Meléndez, M., Kraemer, S. B., & Schmitt, H. R. 2010,
 1229 *MNRAS*, 406, 493, doi: [10.1111/j.1365-2966.2010.16679.x](https://doi.org/10.1111/j.1365-2966.2010.16679.x)
- 1230 Mezcua, M., & Prieto, M. A. 2014, *ApJ*, 787, 62,
 1231 doi: [10.1088/0004-637X/787/1/62](https://doi.org/10.1088/0004-637X/787/1/62)
- 1232 Molina, M., Eracleous, M., Barth, A. J., et al. 2018, *ApJ*,
 1233 864, 90, doi: [10.3847/1538-4357/aad5ed](https://doi.org/10.3847/1538-4357/aad5ed)
- 1234 Müller-Sánchez, F., Prieto, M. A., Hicks, E. K. S., et al.
 1235 2011, *ApJ*, 739, 69, doi: [10.1088/0004-637X/739/2/69](https://doi.org/10.1088/0004-637X/739/2/69)
- 1236 Müller-Sánchez, F., Prieto, M. A., Mezcua, M., et al. 2013,
 1237 *ApJL*, 763, L1, doi: [10.1088/2041-8205/763/1/L1](https://doi.org/10.1088/2041-8205/763/1/L1)
- 1238 Nagar, N. M., Falcke, H., & Wilson, A. S. 2005, *A&A*, 435,
 1239 521, doi: [10.1051/0004-6361:20042277](https://doi.org/10.1051/0004-6361:20042277)
- 1240 Nagar, N. M., Falcke, H., Wilson, A. S., & Ulvestad, J. S.
 1241 2002, *A&A*, 392, 53, doi: [10.1051/0004-6361:20020874](https://doi.org/10.1051/0004-6361:20020874)
- 1242 Narayan, R., & Yi, I. 1995, *ApJ*, 452, 710,
 1243 doi: [10.1086/176343](https://doi.org/10.1086/176343)
- 1244 Nemmen, R. S., Storchi-Bergmann, T., & Eracleous, M.
 1245 2014, *MNRAS*, 438, 2804, doi: [10.1093/mnras/stt2388](https://doi.org/10.1093/mnras/stt2388)
- 1246 Nicastro, F., Martocchia, A., & Matt, G. 2003, *ApJL*, 589,
 1247 L13, doi: [10.1086/375715](https://doi.org/10.1086/375715)
- 1248 Nussbaumer, H., & Osterbrock, D. E. 1970, *ApJ*, 161, 811,
 1249 doi: [10.1086/150585](https://doi.org/10.1086/150585)
- 1250 Oliva, E., Salvati, M., Moorwood, A. F. M., & Marconi, A.
 1251 1994, *A&A*, 288, 457
- 1252 Panessa, F., Barcons, X., Bassani, L., et al. 2007, *A&A*,
 1253 467, 519, doi: [10.1051/0004-6361:20066943](https://doi.org/10.1051/0004-6361:20066943)
- 1254 Park, J., Hada, K., Kino, M., et al. 2019, *ApJ*, 871, 257,
 1255 doi: [10.3847/1538-4357/aaf9a9](https://doi.org/10.3847/1538-4357/aaf9a9)
- 1256 Pellegrini, S., Baldi, A., Fabbiano, G., & Kim, D. W. 2003,
 1257 *ApJ*, 597, 175, doi: [10.1086/378235](https://doi.org/10.1086/378235)
- 1258 Pellegrini, S., Fabbiano, G., Fiore, F., Trinchieri, G., &
 1259 Antonelli, A. 2002, *A&A*, 383, 1,
 1260 doi: [10.1051/0004-6361:20011482](https://doi.org/10.1051/0004-6361:20011482)
- 1261 Pereira-Santaella, M., Álvarez-Márquez, J., García-Bernete,
 1262 I., et al. 2022, *A&A*, 665, L11,
 1263 doi: [10.1051/0004-6361/202244725](https://doi.org/10.1051/0004-6361/202244725)
- 1264 Pier, E. A., & Voit, G. M. 1995, *ApJ*, 450, 628,
 1265 doi: [10.1086/176171](https://doi.org/10.1086/176171)
- 1266 Plotkin, R. M., Anderson, S. F., Brandt, W. N., et al. 2012,
 1267 *ApJL*, 745, L27, doi: [10.1088/2041-8205/745/2/L27](https://doi.org/10.1088/2041-8205/745/2/L27)
- 1268 Pogge, R. W., Maoz, D., Ho, L. C., & Eracleous, M. 2000,
 1269 *ApJ*, 532, 323, doi: [10.1086/308567](https://doi.org/10.1086/308567)
- 1270 Pontoppidan, K. M., Barrientes, J., Blome, C., et al. 2022,
 1271 *ApJL*, 936, L14, doi: [10.3847/2041-8213/ac8a4e](https://doi.org/10.3847/2041-8213/ac8a4e)
- 1272 Porth, O., Chatterjee, K., Narayan, R., et al. 2019, *ApJS*,
 1273 243, 26, doi: [10.3847/1538-4365/ab29fd](https://doi.org/10.3847/1538-4365/ab29fd)
- 1274 Prieto, M. A., Fernández-Ontiveros, J. A., Markoff, S.,
 1275 Espada, D., & González-Martín, O. 2016, *MNRAS*, 457,
 1276 3801, doi: [10.1093/mnras/stw166](https://doi.org/10.1093/mnras/stw166)
- 1277 Prieto, M. A., Mezcua, M., Fernández-Ontiveros, J. A., &
 1278 Schartmann, M. 2014, *MNRAS*, 442, 2145,
 1279 doi: [10.1093/mnras/stu1006](https://doi.org/10.1093/mnras/stu1006)
- 1280 Prieto, M. A., Nadołny, J., Fernández-Ontiveros, J. A., &
 1281 Mezcua, M. 2021, *MNRAS*, 506, 562,
 1282 doi: [10.1093/mnras/stab1704](https://doi.org/10.1093/mnras/stab1704)
- 1283 Prieto, M. A., Reunanen, J., Tristram, K. R. W., et al.
 1284 2010, *MNRAS*, 402, 724,
 1285 doi: [10.1111/j.1365-2966.2009.15897.x](https://doi.org/10.1111/j.1365-2966.2009.15897.x)
- 1286 Ricci, C., Trakhtenbrot, B., Koss, M. J., et al. 2017, *ApJS*,
 1287 233, 17, doi: [10.3847/1538-4365/aa96ad](https://doi.org/10.3847/1538-4365/aa96ad)
- 1288 Rodríguez-Ardila, A., Prieto, M. A., Portilla, J. G., &
 1289 Tejeiro, J. M. 2011, *ApJ*, 743, 100,
 1290 doi: [10.1088/0004-637X/743/2/100](https://doi.org/10.1088/0004-637X/743/2/100)
- 1291 Rodríguez-Ardila, A., Prieto, M. A., Viegas, S., &
 1292 Gruenwald, R. 2006, *ApJ*, 653, 1098, doi: [10.1086/508864](https://doi.org/10.1086/508864)
- 1293 Sajina, A., Lacy, M., & Pope, A. 2022, *Universe*, 8, 356,
 1294 doi: [10.3390/universe8070356](https://doi.org/10.3390/universe8070356)
- 1295 Satyapal, S., Vega, D., Dudik, R. P., Abel, N. P., &
 1296 Heckman, T. 2008, *ApJ*, 677, 926, doi: [10.1086/529014](https://doi.org/10.1086/529014)
- 1297 Sheth, K., Regan, M., Hinz, J. L., et al. 2010, *PASP*, 122,
 1298 1397, doi: [10.1086/657638](https://doi.org/10.1086/657638)
- 1299 Shi, F., Li, Z., Yuan, F., & Zhu, B. 2021, *Nature*
 1300 *Astronomy*, 5, 928, doi: [10.1038/s41550-021-01394-0](https://doi.org/10.1038/s41550-021-01394-0)
- 1301 Sikora, M., Stawarz, L., & Lasota, J.-P. 2007, *ApJ*, 658,
 1302 815, doi: [10.1086/511972](https://doi.org/10.1086/511972)
- 1303 Silk, J., & Rees, M. J. 1998, *A&A*, 331, L1,
 1304 doi: [10.48550/arXiv.astro-ph/9801013](https://doi.org/10.48550/arXiv.astro-ph/9801013)
- 1305 Stern, J., Laor, A., & Baskin, A. 2014, *MNRAS*, 438, 901,
 1306 doi: [10.1093/mnras/stt1843](https://doi.org/10.1093/mnras/stt1843)
- 1307 Sugai, H., Hattori, T., Kawai, A., et al. 2005, *ApJ*, 629,
 1308 131, doi: [10.1086/431544](https://doi.org/10.1086/431544)
- 1309 Terashima, Y., & Wilson, A. S. 2003, *ApJ*, 583, 145,
 1310 doi: [10.1086/345339](https://doi.org/10.1086/345339)
- 1311 Tommasin, S., Spinoglio, L., Malkan, M. A., & Fazio, G.
 1312 2010, *ApJ*, 709, 1257,
 1313 doi: [10.1088/0004-637X/709/2/1257](https://doi.org/10.1088/0004-637X/709/2/1257)
- 1314 Tonry, J. L., Dressler, A., Blakeslee, J. P., et al. 2001, *ApJ*,
 1315 546, 681, doi: [10.1086/318301](https://doi.org/10.1086/318301)
- 1316 Trump, J. R., Impey, C. D., Kelly, B. C., et al. 2011, *ApJ*,
 1317 733, 60, doi: [10.1088/0004-637X/733/1/60](https://doi.org/10.1088/0004-637X/733/1/60)

- 1318 Walsh, J. L., Barth, A. J., Ho, L. C., et al. 2008, *AJ*, 136,
1319 1677, doi: [10.1088/0004-6256/136/4/1677](https://doi.org/10.1088/0004-6256/136/4/1677)
- 1320 Wang, Q. D., Nowak, M. A., Markoff, S. B., et al. 2013,
1321 *Science*, 341, 981, doi: [10.1126/science.1240755](https://doi.org/10.1126/science.1240755)
- 1322 Weinberger, R., Springel, V., Hernquist, L., et al. 2017,
1323 *MNRAS*, 465, 3291, doi: [10.1093/mnras/stw2944](https://doi.org/10.1093/mnras/stw2944)
- 1324 Wells, M., Pel, J. W., Glasse, A., et al. 2015, *PASP*, 127,
1325 646, doi: [10.1086/682281](https://doi.org/10.1086/682281)
- 1326 Wilson, A. S., & Raymond, J. C. 1999, *ApJL*, 513, L115,
1327 doi: [10.1086/311923](https://doi.org/10.1086/311923)
- 1328 Wrobel, J. M. 1984, *ApJ*, 284, 531, doi: [10.1086/162436](https://doi.org/10.1086/162436)
- 1329 Xue, Y. Q., Luo, B., Brandt, W. N., et al. 2016, *ApJS*, 224,
1330 15, doi: [10.3847/0067-0049/224/2/15](https://doi.org/10.3847/0067-0049/224/2/15)
- 1331 Yuan, F., Bu, D., & Wu, M. 2012, *ApJ*, 761, 130,
1332 doi: [10.1088/0004-637X/761/2/130](https://doi.org/10.1088/0004-637X/761/2/130)
- 1333 Yuan, F., Gan, Z., Narayan, R., et al. 2015, *ApJ*, 804, 101,
1334 doi: [10.1088/0004-637X/804/2/101](https://doi.org/10.1088/0004-637X/804/2/101)
- 1335 Yuan, F., & Narayan, R. 2014, *ARA&A*, 52, 529,
1336 doi: [10.1146/annurev-astro-082812-141003](https://doi.org/10.1146/annurev-astro-082812-141003)